



# Retrieval of atmospheric CO<sub>2</sub> vertical profiles from ground-based near-infrared spectra

Sébastien Roche<sup>1</sup>, Kimberly Strong<sup>1</sup>, Debra Wunch<sup>1</sup>, Joseph Mendonca<sup>2</sup>, Colm Sweeney<sup>3</sup>, Bianca Baier<sup>4,3</sup>, Sébastien C. Biraud<sup>5</sup>, Joshua L. Laughner<sup>6</sup>, Geoffrey C. Toon<sup>7</sup>, and Brian J. Connor<sup>8</sup>

<sup>1</sup>Department of Physics, University of Toronto, Toronto, ON, Canada

<sup>2</sup>Climate Research Division, Environment and Climate Change Canada, Toronto, ON, Canada

<sup>3</sup>NOAA Global Monitoring Laboratory, Boulder, CO, USA

<sup>4</sup>Cooperative Institute for Research in Environmental Sciences, University of Colorado, Boulder, CO, USA

<sup>5</sup>Lawrence Berkeley National Laboratory, Berkeley, CA, USA

<sup>6</sup>Division of Geological and Planetary Sciences, California Institute of Technology, Pasadena, CA, USA

<sup>7</sup>Jet Propulsion Laboratory, California Institute of Technology, Pasadena, CA, USA

<sup>8</sup>BC Consulting Limited, Martinborough, New Zealand

**Correspondence:** Sébastien Roche (sebastien.roche@mail.utoronto.ca)

Received: 26 October 2020 – Discussion started: 13 November 2020

Revised: 7 March 2021 – Accepted: 22 March 2021 – Published: 28 April 2021

**Abstract.** We evaluate vertical profile retrievals of CO<sub>2</sub> from 0.02 cm<sup>-1</sup> resolution ground-based near-infrared solar absorption spectra with the GFIT2 algorithm, using improved spectroscopic line lists and line shapes. With these improvements, CO<sub>2</sub> profiles were obtained from sequential retrievals in five spectral windows with different vertical sensitivities using synthetic and real spectra. A sensitivity study using synthetic spectra shows that the leading source of uncertainty in the retrieved CO<sub>2</sub> profiles is the error in the a priori temperature profile, even with 3-hourly reanalysis a priori profiles. A 2 °C error in the temperature profile in the lower troposphere between 0.6 and 0.85 atm causes deviations in the retrieved CO<sub>2</sub> profiles that are larger than the typical vertical variations of CO<sub>2</sub>. To distinguish the effect of errors in the a priori meteorology and trace gas concentration profiles from those in the instrument alignment and spectroscopic parameters, we retrieve CO<sub>2</sub> profiles from atmospheric spectra while using an a priori profile built from coincident AirCore, radiosonde, and surface in situ measurements at the Lamont, Oklahoma (USA), Total Carbon Column Observing Network station. In those cases, the deviations in retrieved CO<sub>2</sub> profiles are also larger than typical vertical variations of CO<sub>2</sub>, suggesting that remaining errors in the forward model limit the accuracy of the retrieved profiles. Implementing a temperature retrieval or correction and quantifying and model-

ing an imperfect instrument alignment are critical to improve CO<sub>2</sub> profile retrievals. Without significant advances in modeling imperfect instrument alignment, and improvements in the accuracy of the temperature profile, the CO<sub>2</sub> profile retrieval with GFIT2 presents no clear advantage over scaling retrievals for the purpose of ascertaining the total column.

## 1 Introduction

Carbon dioxide (CO<sub>2</sub>) is the most abundant well-mixed greenhouse gas in the atmosphere and the main driver of the increase in global mean surface temperatures since the start of the industrial era (Ciais et al., 2013; Myhre et al., 2013). A yearly global carbon budget has been produced by the Global Carbon Project since 2012 (Friedlingstein et al., 2019; Le Quéré et al., 2013, 2014, 2015b, a, 2016, 2018b, a). It presents current knowledge of CO<sub>2</sub> emissions to inform policies that aim to reduce the emissions of greenhouse gases into the atmosphere. The project uses ensembles of models and inventories, as well as CO<sub>2</sub> surface measurements, to estimate different components of the global emissions of CO<sub>2</sub>. It also uses CO<sub>2</sub> fluxes obtained from atmospheric inversions (Chevallier et al., 2005; van der Laan-Luijkx et al., 2017; Rödenbeck et al., 2003; Saeki and Patra, 2017) as a

semi-independent validation tool for these estimates; most of the CO<sub>2</sub> measurements used in these inversions come from surface networks. Since 2014, the project makes mention of the potential of inversions using space-based measurements of total column CO<sub>2</sub> to provide additional constraints on sources and sinks of CO<sub>2</sub>.

Column-averaged dry-air mole fractions of CO<sub>2</sub> (XCO<sub>2</sub>), are retrieved from solar absorption spectra measured from space by the Atmospheric InfraRed Sounder (AIRS, Aumann et al., 2003), the Greenhouse gases Observing SATellite (GOSAT and GOSAT-2) (Kuze et al., 2009, 2016; Nakajima et al., 2012), the Orbiting Carbon Observatory (OCO-2 and OCO-3) (Crisp, 2008, 2015; Eldering et al., 2019), and Tansat (Liu et al., 2018). CO<sub>2</sub> fluxes obtained from inversions assimilating OCO-2 observations over land are now becoming as reliable as those obtained from inversions using surface air sampling networks (Chevallier et al., 2019). Measurements of XCO<sub>2</sub> by satellites can be made with unprecedented spatial coverage. Inversions using CO<sub>2</sub> total columns over land are less sensitive to transport errors than inversions using surface CO<sub>2</sub> (Basu et al., 2018; Rayner and O'Brien, 2001), which require accurate modeling of the planetary boundary layer height and vertical mixing, both of which are a major source of uncertainty in inversions (Parazoo et al., 2012). However, even small (< 1 ppm) spatially coherent biases in column measurements can have a large impact on inversions assimilating XCO<sub>2</sub> (Chevallier et al., 2007), and efforts must be made to characterize and minimize such biases (Kiel et al., 2019; O'Dell et al., 2018).

The Total Carbon Column Observing Network (TCCON) is a ground-based network of high-resolution (0.02 cm<sup>-1</sup>) ground-based Fourier transform infrared (FTIR) spectrometers that record shortwave IR (SWIR) solar absorption spectra (Wunch et al., 2011b). TCCON produces retrievals of XCO<sub>2</sub> which are widely used to validate satellite observations and to study the carbon cycle (Wunch et al., 2011a, 2017; Keppel-Aleks et al., 2012, 2013). New versions of the TCCON retrieval algorithm (GGG) are released every few years, and each new version is designed to improve the quality of the data.

GGG2014 (Wunch et al., 2015) is the current version of the GGG software used by TCCON to transform measured interferograms into spectra, and then to retrieve trace gas mixing ratios from those spectra. Central to this process is GFIT, a non-linear least-squares spectral fitting algorithm. A forward model computes an atmospheric transmittance spectrum for a given observation geometry using a priori knowledge of atmospheric conditions and assuming a perfectly aligned instrument. An inverse method then compares the measured spectrum with the resulting calculation and adjusts the retrieved parameters to obtain the best fit. In GFIT, these parameters include volume mixing ratio scaling factors (VSFs) for the different fitted gases. GFIT performs profile scaling retrievals: for each retrieved trace gas, a single VSF scales the entire a priori concentration profile at all alti-

tude levels simultaneously and therefore the retrieved profile shape is unchanged from the a priori profile shape. Technically, GFIT handles the scaling retrieval by weakly constraining the fitted VSF factor. The approach is equivalent to performing an optimal estimation of the VSF, assigning a value of unity to the a priori VSF and a value of 10<sup>6</sup> as its expected range of variability. XCO<sub>2</sub> can be retrieved with a 2σ precision and accuracy of 0.8 ppm (Wunch et al., 2010). GFIT minimizes the spectral fit residuals: the difference between the measured and calculated spectra. The measurement noise is not required to be accurately known; all retrievals from TCCON CO<sub>2</sub> windows use an assumed signal-to-noise ratio (SNR) of ~200. This assumption has only a small effect on the result because for CO<sub>2</sub> the absorption line depths and the spectral fitting residuals far exceed the measurement noise.

Even though TCCON XCO<sub>2</sub> observations are precise and accurate, they explicitly lack information about the vertical distribution of CO<sub>2</sub> in the atmosphere, which is of interest for the validation of satellite measurements and model simulations and could improve the ability of atmospheric inversions to resolve emissions at regional scales (Keppel-Aleks et al., 2011). The most precise and accurate sources of information on CO<sub>2</sub> vertical profiles are provided by air samples collected at different altitudes using weather balloons or aircraft, but these observations are sparse in space and time. Aircraft vertical profiles are used as validation tools for inversion studies (Peters et al., 2007; Stephens et al., 2007; Pickett-Heaps et al., 2011), which requires them to remain independent from the inversion systems (Chevallier et al., 2019). Obtaining reliable CO<sub>2</sub> profile information from ground-based direct-sun measurements could significantly augment the number of observations available for verification and assimilation in atmospheric inversions, and would allow TCCON to be used for validation of thermal infrared satellite products, e.g., from AIRS and GOSAT/2, and vertically resolved NIR GOSAT and OCO-2 experimental products. Vertical profile information derived from ground-based absorption spectra cannot be as accurate as aircraft-based vertical profiles, and would also be spatially sparse, but would provide a higher temporal sampling.

CO<sub>2</sub> profile retrievals from ground-based SWIR spectra have been calculated using the band centered at 1.6 μm with a Voigt line shape (Kuai et al., 2012), and in the band centered at 2.06 μm with the PROFFIT optimal estimation software package (Hase et al., 2004) fitted with a Voigt line shape with line mixing (Dohe, 2013). In our approach, we use the GFIT2 software package initially described by Connor et al. (2016), which is a profile retrieval algorithm based on the GGG software suite, but modified such that it allows the profile shape to vary during the retrieval process. Instead of retrieving a single VSF value that scales the whole a priori profile, a VSF value is retrieved for each atmospheric level. The algorithm thus has much more freedom to fit the observed spectra but is also more sensitive to uncertainties in the forward model calculations such as errors in the atmospheric temperature

profile, spectroscopic errors, and instrument misalignment, for example.

Connor et al. (2016) showed that CO<sub>2</sub> profile retrievals in the CO<sub>2</sub> band centered at 1.6 μm are very sensitive to errors in spectroscopy. GFIT2 was first developed using the GGG2014 version of the GGG suite (Wunch et al., 2015), which uses a Voigt line shape to compute absorption coefficients. In this study, we use the GGG2020 version, which will be released in early 2021. This version of the code implements quadratic speed-dependent Voigt line shapes with line mixing (qSDV+LM) for CO<sub>2</sub> (Mendonca et al., 2016) and CH<sub>4</sub> (Mendonca et al., 2017) bands, and qSDV line shapes for O<sub>2</sub> in the band centered at 1.27 μm (Mendonca et al., 2019). The line mixing coefficients are derived with the first-order Rosenkranz approximation (Rosenkranz, 1975). This leads to significantly better spectral fits, especially in the strong CO<sub>2</sub> band centered at 2.06 μm, and smaller variations of gas amount with air mass. Other improvements to the forward model include (1) updates to the spectroscopic line list (Toon, 2015) (2) a solar-gas stretch fitted to account for Doppler-driven differences between solar and telluric wavenumber scales (in GGG2014 only the stretch in the telluric wavenumber scale was fitted), and (3) improved a priori profiles as described in Sect. 2.2.

This study assesses the quality of CO<sub>2</sub> profile retrievals with GFIT2 implemented in GGG2020. Section 2 describes the retrieval algorithm and our methodology. Section 3 presents a sensitivity study using synthetic spectra, followed by retrievals using real measured spectra. Finally, Sect. 4 presents a summary of the results and conclusions.

## 2 Methods

In this study, GFIT2 is used to retrieve CO<sub>2</sub> profiles from the two original TCCON retrieval windows and three new windows that possess a large range of opacities, and therefore vertical sensitivities. These windows are presented in Table 1 and Fig. 1. The TCCON1 window (centered at 6220 cm<sup>-1</sup>) and TCCON2 window (centered at 6339.5 cm<sup>-1</sup>) are used to derive XCO<sub>2</sub> in the public TCCON data products, because the spectral absorption line opacities are close to 1 and are therefore equally sensitive at most altitudes. The CO<sub>2</sub> line intensities in the weak windows are 10 times smaller than in the standard TCCON windows, providing more sensitivity to CO<sub>2</sub> variations aloft. The CO<sub>2</sub> lines in the “Strong” window are 15 times stronger than those in the standard TCCON windows, providing more sensitivity to CO<sub>2</sub> variations near the surface. All windows have an average lower-state energy ( $E''$ ) of roughly 240 cm<sup>-1</sup>, rendering the retrieved total column of CO<sub>2</sub> highly independent of the assumed temperature (< 0.1 % K<sup>-1</sup>). The derivation of XCO<sub>2</sub> as calculated in GGG is described in Appendix A. XCO<sub>2</sub> is the ratio of the CO<sub>2</sub> column to the column of dry air, and the column of dry air is expressed as the retrieved O<sub>2</sub> column (from

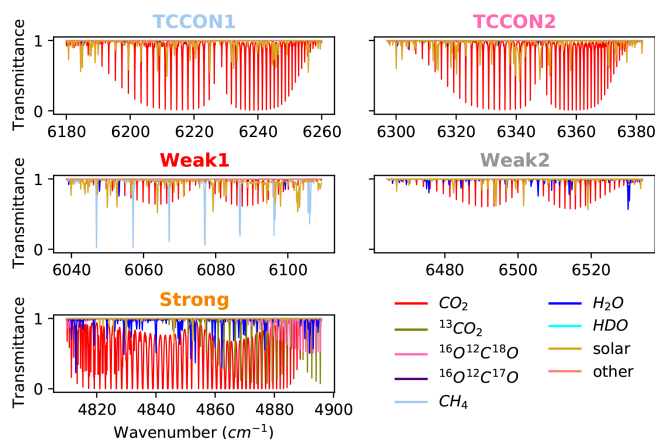


**Figure 1.** Contributions of different absorbing gases to the calculated transmittance spectrum on a dry winter day at a solar zenith angle of 60.6° for each of the spectral windows used to retrieve CO<sub>2</sub>.

the window centered at 7885 cm<sup>-1</sup>; see Table 1) divided by 0.2095 (Wunch et al., 2011b). OCO-2/3 and GOSAT/2 use two windows comparable to the TCCON1 and Strong windows to retrieve CO<sub>2</sub> and use the O<sub>2</sub> A-band (centered near 13158 cm<sup>-1</sup>).

A qualitative representation of the vertical sensitivity due to the range of different line opacities is presented in Fig. 2, which shows the normalized CO<sub>2</sub> Jacobian for typical absorption lines in the Strong window (centered at 4852.87 cm<sup>-1</sup>), the “Weak1” window (centered at 6074 cm<sup>-1</sup>), and the TCCON1 window (centered at 6220 cm<sup>-1</sup>). The strong saturated lines of the Strong window are more sensitive to levels below 5 km than in the TCCON1 window, but the Strong window also contains lines of intermediate absorption strength that provide more uniform sensitivity up to ~ 10 km, and that extend the window’s sensitivity to up to 30–40 km. The saturated lines in the Strong window correspond to the 20013–00001 band, while the lines of intermediate strength around 4820 cm<sup>-1</sup> come from the R branch of the 21113–01101 band. The TCCON1 window has more uniform sensitivity up to ~ 10–15 km and contains weak lines which contain information on CO<sub>2</sub> above 15 km. The Weak1 window is less sensitive below 10 km and has more uniform sensitivity between 10–20 km. Figure 2 also shows little to no sensitivity to levels above ~ 30 km in all windows.

### 2.1 Retrieval algorithm

The GFIT2 retrieval algorithm is described in detail in Appendix B and follows the formulation of Rodgers (2000). Currently, GGG has no option to simultaneously retrieve information about a gas from spectral windows that are not contiguous in wavenumber. Therefore, we retrieve trace gas information from each window separately. We see no ad-

**Table 1.** CO<sub>2</sub> spectral windows used with GFIT2. Interfering absorbers labeled “solar” are due to absorption by heavy metal ions (e.g., Fe, Si, Ca, Ni) in the solar photosphere. Also shown are the strength-weighted averages of the lower-state energy ( $E''$ ) and of the line strengths ( $S$ ) over all the CO<sub>2</sub> lines in each window. The column of O<sub>2</sub>, retrieved with scaling retrievals from the O<sub>2</sub> window, is used to compute XCO<sub>2</sub>.

Window name	Center (μm)	Center (cm <sup>-1</sup> )	Width (cm <sup>-1</sup> )	Primary interfering absorbers	$E''$ (cm <sup>-1</sup> )	$S$ (cm <sup>-1</sup> (molecule cm <sup>-2</sup> ) <sup>-1</sup> ) × 10 <sup>-23</sup>
TCCON1	1.61	6220	80	solar, H <sub>2</sub> O	245.3	1.14
TCCON2	1.58	6339.5	85	solar, H <sub>2</sub> O	254.6	1.14
Weak1	1.65	6074	70.8	CH <sub>4</sub> , solar, H <sub>2</sub> O	223.5	0.118
Weak2	1.54	6499.1	69.8	solar, H <sub>2</sub> O, HDO	229.3	0.130
Strong	2.06	4852.87	86.26	H <sub>2</sub> O, <sup>13</sup> CO <sub>2</sub> , solar	243.8	17.8
O <sub>2</sub>	1.27	7885	240	solar, H <sub>2</sub> O, HF, CO <sub>2</sub>	203.4	0.00518

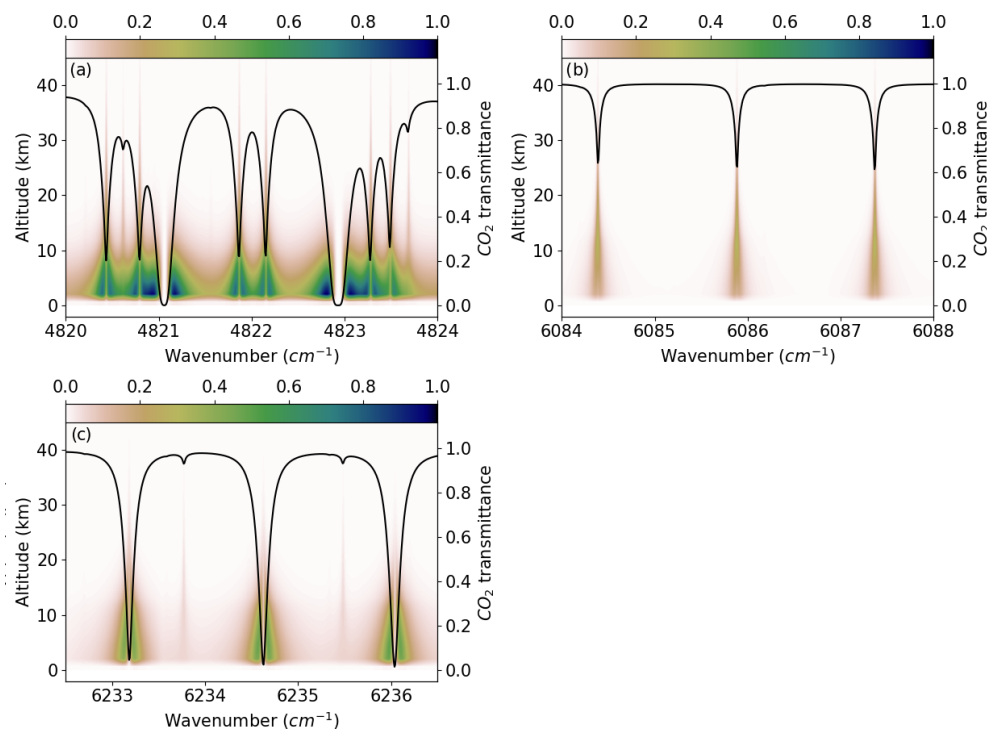


**Figure 2.** CO<sub>2</sub> absorption lines (black line) overlaid on heat maps of the CO<sub>2</sub> Jacobian for lines of (a) the Strong window, (b) the Weak1 window, and (c) the TCCON1 window. The color bar represents the normalized Jacobian where 1 corresponds to the maximum amongst all the CO<sub>2</sub> Jacobians from the five CO<sub>2</sub> windows. Lines of the Weak2 and TCCON2 windows are not shown as they look like the Weak1 and TCCON1 windows, respectively.

vantage to fitting non-contiguous windows simultaneously, rather than separately, and then combining the results. In TCCON post-processing, the total columns retrieved from different retrieval windows (CO<sub>2</sub> from the TCCON1 and TCCON2 windows, for example) are averaged after removing window-dependent multiplicative biases, using retrieval errors as weights. Table 2 summarizes the components of the state vector used in GFIT2. A total of 51 VSFs are retrieved (one for each atmospheric level) for the primary target gas, while only 1 VSF is retrieved for each of the interfering

species profiles (non-<sup>12</sup>C<sup>16</sup>O<sub>2</sub> species included in Fig. 1, except for “solar” and “other”; other CO<sub>2</sub> isotopologues are only retrieved as interfering species in the Strong window). Aside from the retrieved gases, other fitted parameters are part of the state vector. Orthogonal continuum basis functions are used to fit the shape of a spectrum’s continuum, with different orders of curvature. An overall frequency stretch is retrieved for all lines, and a second “solar-gas” stretch is retrieved to correct for differences between the solar and tel-

**Table 2.** Components of the state vector in GFIT2 profile retrievals. These are all the retrieved parameters.

State vector parameter	Number of elements
Main target gas (CO <sub>2</sub> )	51 (number of atmospheric levels)
Interfering species	3–6 (scaling retrievals)
Continuum basis functions	$N$ (5 in the Strong window, 3 in the other windows)
Continuum level	1
Continuum tilt	1
Continuum curvature	$N - 2$
Frequency stretch	1
Solar-gas stretch	1
Zero-level offset	0 (1 in the Strong window)

luric wavenumber scales. A zero-level offset is also retrieved in the Strong window that makes use of saturated lines.

In principle, a CO<sub>2</sub> profile retrieval should have little sensitivity to errors in the a priori CO<sub>2</sub> profile (differences from the true profile) since it can adjust for differences between measured and calculated spectra caused by erroneous prior profile shapes (Connor et al., 2016). However, the retrieval may also conflate errors due to other sources, such as incorrect spectroscopic parameters, incorrect modeling of the instrument line shape, or errors in the a priori meteorology and profiles of interfering species, with these errors in the a priori CO<sub>2</sub> profile.

## 2.2 Datasets

CO<sub>2</sub> and CH<sub>4</sub> a priori profiles were built by combining the balloon-borne AirCore (Karion et al., 2010) profiles with surface in situ measurements, adding the GGG2020 a priori profile above the maximum altitude sampled by AirCore. These composite profiles will be referred to as “truth”. The CH<sub>4</sub> profile is included because CH<sub>4</sub> is an interfering gas in the Weak1 window. AirCore is a sampling system that consists of a long, coiled stainless-steel tube initially filled with a dry calibrated gas. As a balloon carries it up, the fill gas evacuates. When the AirCore descends from the stratosphere, ambient air enters the tube through the open end. Upon landing, the AirCore is quickly retrieved for subsequent laboratory analysis, wherein the sample is pushed through a continuous gas analyzer. The first gases to come out were the last to enter, and vice versa, allowing the preserved atmospheric trace gas concentration profiles to be derived. This method has precision similar to, or better than, discrete gas flask samples, with a repeatability of 0.07 ppm for CO<sub>2</sub> concentrations (Karion et al., 2010). The balloons reach  $\sim 30$  km altitude, with profiles retrieved to  $\sim 25$  km, and therefore sample 98 %

**Table 3.** AirCore launch dates and number of coincident spectra within  $\pm 1$  h of the AirCore last sampling time and within  $\pm 1.5$  h of the closest a priori time. The range of solar zenith angles covered by the coincident spectra is also shown.

Launch date	Coincident spectra	Solar zenith angles (°)
14 January 2012	65	60.6–73.8
15 January 2012	48	65.6–77.9
23 July 2013	44	20.8–36.5
26 February 2014	61	46.6–59.0
27 February 2014	41	46.2–53.3
17 September 2014	48	37.9–51.1
19 October 2016	31	47.1–50.3
11 April 2017	33	31.2–39.2

of the mass of the atmosphere. In Sect. 3.2, AirCore profiles from the v20181101 dataset were used as “truth” to assess the quality of GFIT2 profile retrievals. We used all AirCore profiles measured over the Lamont TCCON station that had coincident ground-based measurements within  $\pm 1$  h of the AirCore landing and within  $\pm 1.5$  h of the closest a priori time. All figures showing profiles use the average of profiles retrieved from the coincident spectra. The launch dates of the eight AirCore profiles used are presented in Table 3. An iMet-1 radiosonde carried by the same balloon as the AirCore provides in situ temperature and relative humidity profiles.

Instead of the diagonal prior covariance used in Sect. 3.1, a more realistic CO<sub>2</sub> prior covariance matrix was built for retrievals with real spectra in Sect. 3.2. The difference between GGG2020 a priori CO<sub>2</sub> profiles and aircraft profiles (Biraud et al., 2013) over Lamont from NOAA’s ObsPack (Sweeney et al., 2017) between 500 and 5000 m were computed for 382 aircraft profiles and for each month between 2008 and 2016. The mean difference profile plus 1 standard deviation of the month with the largest differences, August, was used to build the diagonal of the a priori covariance matrix. The a priori CO<sub>2</sub> uncertainty can be expressed as

$$\sigma_i = 3.99e^{-0.92x_i} + 0.98, \quad (1)$$

where  $x$  is the altitude of the  $i$ th atmospheric level in kilometers. The a priori covariance is expressed as

$$\mathbf{z}_{i,j} = \mathbf{x}_i, \quad (2)$$

$$(\Delta\mathbf{z})_{i,j} = \left| \mathbf{z}_{i,j} - \mathbf{z}_{i,j}^T \right|, \quad (3)$$

$$(\mathbf{S}_a)_{i,j} = \left( \sigma^T \sigma \right)_{i,j} \times e^{-\frac{(\Delta\mathbf{z})_{i,j}}{h}}, \quad (4)$$

where  $\mathbf{z}$  is a matrix with each row containing the altitude profile,  $\Delta\mathbf{z}$  is the matrix of absolute altitude differences between each level,  $\mathbf{S}_a$  is the a priori covariance matrix, and  $h$  is the length scale of interlayer correlations. The length scale was

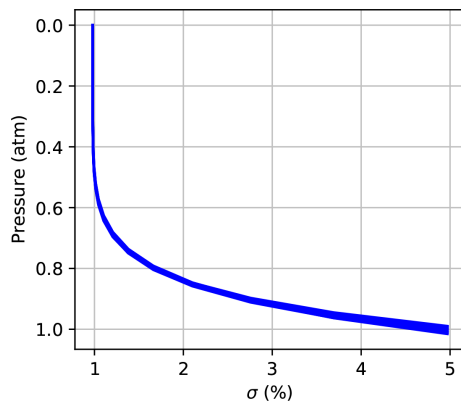


**Figure 3.** A priori uncertainty profiles for each of the 10 dates presented in Table 3. These are defined by Eq. (1). Since  $\sigma$  is defined on an altitude grid, it varies slightly with pressure.

set to 2 km based on the width of the rows of correlation matrices built from the ensemble of aircraft vertical profiles.

The vertical grid used in the retrievals presented in this study has 51 levels between 0 and 70 km, and the spacing between levels increases with altitude (see Appendix A). Figure 3 shows the a priori uncertainty as a function of pressure for each of the eight a priori states used to process the Lamont spectra presented in Table 3.

Since the AirCore profiles do not extend down to the surface or above about 25 km, other sources are used to complete the “true” CO<sub>2</sub> profile. The TCCON spectrometer used in this study is located at the US Department of Energy Atmospheric Radiation Measurement program (ARM) central facility in Lamont, Oklahoma. The facility hosts a suite of instruments for remote and in situ measurements of the atmosphere. When available within 5 h of the last AirCore sampling time, surface CO<sub>2</sub> and CH<sub>4</sub> measurements from precision gas systems were used (Biraud and Moyes, 2001). When they were not available, measurements from discrete flask samples were used (on 23 July 2013, 27 February 2014, and 17 September 2014) (Biraud et al., 2002). Surface pressure, temperature, and relative humidity were obtained from in situ measurements at the Lamont central facility.

GGG2020 uses 3-hourly a priori profiles of the atmospheric state. For each spectrum in the retrievals, GGG uses the nearest a priori profile in time. The a priori meteorology and H<sub>2</sub>O profiles are obtained from analyses of the Global Modeling and Assimilation Office (GMAO) Goddard Earth Observing System Version 5 Forward Processing for Instrument Teams (GEOS5-FPIT) (Lucchesi, 2015). The CO<sub>2</sub> a priori profiles are constructed from the deseasonalized NOAA Mauna Loa and Samoa flask data (Dlugokencky et al., 2019) by determining the transport lag between the measurement site and each level of the a priori profile (Laughner et al., 2021a, b). In the troposphere, this is done with an age-of-air formula and an effective latitude that accounts for synoptic motion of air. In the stratosphere, this is

obtained from an age climatology derived from a chemical Lagrangian model (McKenna, 2002) of the stratosphere using equivalent latitude to account for air motion. The stratospheric priors also account for turbulent mixing with age spectra (Andrews et al., 2001). A seasonal cycle parametrization is then applied, and the resulting CO<sub>2</sub> profiles are corrected to match the CO<sub>2</sub> latitudinal gradients observed by the High-Performance Instrumented Airborne Platform for Environmental Research (HIAPER) Pole-to-Pole Observations (HIPPO) (Wofsy, 2011) and by the Atmospheric Tomography (ATom) mission (Wofsy et al., 2018).

### 2.3 Information content and degrees of freedom

The information content in the profile retrieval can be quantified using the averaging kernel matrix  $\mathbf{A}$  (Rodgers, 2000). The information content  $H$  is defined as

$$H = -\frac{1}{2} \ln(|\mathbf{I} - \mathbf{A}|), \quad (5)$$

where “ln” is the natural logarithm and  $|\mathbf{I} - \mathbf{A}|$  is the determinant of the difference between the identity matrix and the averaging kernel matrix. The degrees of freedom for signal (DOFs) can be expressed as

$$\text{DOFs} = \text{tr}(\mathbf{A}). \quad (6)$$

The DOFs can be divided into the CO<sub>2</sub> profile DOFs and the DOFs corresponding to the rest of the state vector elements. The profile DOFs can be interpreted as the number of independent pieces of information that improve the retrieved CO<sub>2</sub> profiles compared to the a priori profile. The DOFs are shown in Figs. 4–7 and 9–10.

## 3 Results

In Sect. 3.1, we investigate the sensitivity of the profile retrievals to different sources of error using synthetic spectra produced by running the GGG forward model with a given set of atmospheric conditions. The resulting spectra were then used as input to the profile retrieval algorithm using the same set of atmospheric conditions, except for a perturbation in either the CO<sub>2</sub>, temperature, or H<sub>2</sub>O profiles, or in the spectroscopic parameters of CO<sub>2</sub> lines (air- and self-broadened half-width coefficients and their temperature dependence). In these retrievals, the SNR of the spectrum to be fitted is set to 1000 and the CO<sub>2</sub> a priori covariance matrix is diagonal with 5 % ( $\sim 20$  ppm) uncertainty at all levels. No noise is added to the calculated spectra, but the assumed 1000:1 SNR is used to build the measurement covariance matrix and affects the relative weight of the measurement and the a priori profile. The weak prior constraint and high SNR serve to highlight the sources of variability in the retrieved profiles.

In Sect. 3.2, CO<sub>2</sub> profile retrievals are tested with atmospheric solar absorption spectra measured at the TCCON site

in Lamont, Oklahoma (USA). If the forward model were perfect and the a priori state equal to the true state of the atmosphere, the retrieved scale factor at each level would be equal to 1. However, errors in the forward model (including spectroscopy, a priori meteorological information, radiative transfer, and instrument line shape) cause the retrieved scale factors to deviate from 1. To isolate the effect of instrument misalignment and errors in spectroscopic parameters from errors in a priori meteorology, we build a priori profiles of H<sub>2</sub>O, temperature, CO<sub>2</sub>, and CH<sub>4</sub> using in situ measurements. In Sect. 3.2 we also use an a priori covariance matrix with off-diagonal elements based on comparisons between the a priori profile and aircraft profiles, as described in Sect. 2.2.

### 3.1 Synthetic spectra

In this section, we attempt to identify the main sources of error in the retrieved CO<sub>2</sub> profiles. To do this we use synthetic spectra that are calculated with GFIT's forward model for a given set of inputs (atmospheric conditions and spectroscopic parameters). These “perfect” synthetic spectra are then used as measurements to be fitted in retrievals with one perturbed input. Thus, when the perturbed input is not the a priori CO<sub>2</sub> profile itself, the a priori CO<sub>2</sub> profile is the “truth”. In Sect. 3.1.1, we look at the ability of the retrieval algorithm to retrieve CO<sub>2</sub> when it is the only unknown.

Over the course of a day, the water vapor profile can vary by 40% and the temperature profile can vary by more than 10 °C in the lowest troposphere, and therefore 3-hourly a priori meteorological information could differ from the true atmospheric state by several degrees Celsius for temperature and by 10% for water vapor. In Sect. 3.1.2, we perturb the a priori H<sub>2</sub>O profile, the main interfering absorber. In Sect. 3.1.3, we perturb the temperature profile, as the intensity and width of all absorption lines depend on temperature. Finally, in Sect. 3.1.3 we perturb spectroscopic line parameters themselves to within their uncertainties.

The total retrieval random error for the retrievals presented in this section is ~4.5% (~18 ppm), and the contribution of random noise is ~0.8% (~3 ppm); see Appendix D for definitions of total and measurement noise errors. When the deviations from the truth are larger than the a priori uncertainty (~20 ppm), it means the perturbation applied has a severe effect on the retrieval. Of course this can be mitigated by using a stronger a priori constraint or a measurement covariance matrix that reflects expected systematic errors, and not just random noise, but always at the cost of reduced sensitivity to CO<sub>2</sub> too. The goal here is to estimate the relative effect of different kinds of expected systematic errors on retrieved profile shapes. Stronger constraints can only reduce the amplitude of the deviations from the truth, but the same structures would remain. When the perturbation to a parameter other than CO<sub>2</sub> results in deviations from the truth much larger than those presented in Sect. 3.1.1, it means that errors

in that parameter will dominate the variability in the retrieved CO<sub>2</sub> profiles regardless of the retrieval constraints.

#### 3.1.1 Perturbed CO<sub>2</sub> profile

With a perturbed CO<sub>2</sub> prior profile, the algorithm can retrieve the true profile shape very well in all windows, even with an a priori profile vastly different from the truth as shown in Fig. 4. In Fig. 4a, when using the same prior that generated the synthetic spectrum, the retrieved profiles do not align exactly with the prior profile. This is due to small imperfections in the synthetic spectra, but these result in differences of less than 1 ppm at any altitude. In Fig. 4c the standard GGG2020 a priori profile is used as the a priori profile, while the “true” CO<sub>2</sub> profile used to generate the synthetic spectrum was built from a composite “true” profile as described in Sect. 2.2. In each window the retrieved profile is within 2 ppm of the truth. In Fig. 4e a constant CO<sub>2</sub> profile with 380 ppm at all levels is used as the a priori profile. Again, the retrieved profiles are within 2 ppm of the truth except at the bottom and top of the profile where most of the information comes from the a priori profile. This self-consistency test shows that the GFIT2 algorithm works as expected and can accurately retrieve CO<sub>2</sub> when the a priori CO<sub>2</sub> profile is the only source of uncertainty.

#### 3.1.2 Perturbed H<sub>2</sub>O profile

Figure 5 shows the effect of a +10% perturbation to the H<sub>2</sub>O vapor profile below 5 km for a dry winter day and a wet summer day. It leads to 2 ppm deviations from the CO<sub>2</sub> a priori profile in the Strong window under dry conditions and up to 15 ppm under wet conditions. In both cases, the deviations from the truth in the CO<sub>2</sub> profiles retrieved from the other windows were within 2 ppm.

#### 3.1.3 Perturbed temperature profile

A +5 °C perturbation to the temperature profile below 5 km (0.5 atm <  $P$  < 1.0 atm), as in Fig. 6a, leads to deviations from the truth in the retrieved CO<sub>2</sub> profiles of up to 50 ppm in the Weak and TCCON windows, and up to 100 ppm in the Strong window. In that case the fit residuals can exceed 1% in the Strong window and 0.5% in the TCCON windows. For the retrievals used to obtain the profiles in Fig. 6a the SNR was set to 100 in the Strong window, 200 in the TCCON windows, and 1000 in the Weak windows. In Fig. 6c and e the SNR is set to 1000 in all windows. In Fig. 6c, a +2 °C perturbation is applied between 8 and 13 km (0.2 atm <  $P$  < 0.35 atm). The amplitude of deviations in the TCCON windows and in the Strong window is close to 50 ppm at ~0.9 atm and 100 ppm at ~0.2 atm. In the two Weak windows, the deviation amplitude is ~10 ppm at ~0.9 atm and ~20 ppm at 0.2 atm. In Fig. 6e, a +2 °C perturbation is applied above 15 km. In the Strong window, the resulting deviation at pressures > 0.6 atm has the smallest

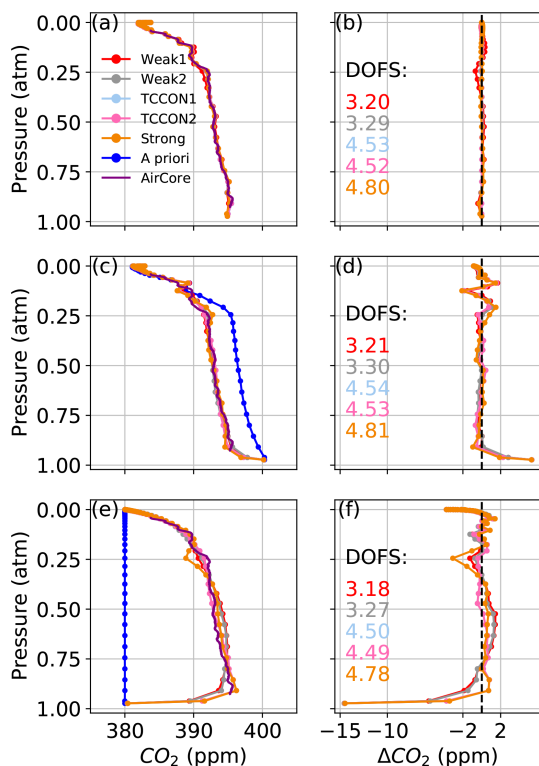


**Figure 4.** The left-hand panels show CO<sub>2</sub> profiles retrieved using synthetic spectra. In (a), we use the AirCore profile, which was used to generate the synthetic spectra, as the a priori profile. In (c), we use the GGG2020 a priori CO<sub>2</sub> profile as the a priori profile. In (e), we use a constant CO<sub>2</sub> a priori profile. Panels (b), (d), and (f) show the difference between the retrieved profiles and AirCore, corresponding to (a), (c), and (e) respectively.

amplitude amongst the five windows, within 4 ppm, and the deviation at  $\sim 0.2$  atm is  $\sim 20$  ppm. In the TCCON windows, the deviation at pressures  $> 0.6$  atm is reduced to  $\sim 10$  ppm while the deviation at pressures  $> 0.6$  atm is comparable to that in Fig. 6b. In the two Weak windows, the deviation at  $\sim 0.9$  atm is unchanged when compared to Fig. 6b and the deviation at  $\sim 0.2$  atm is reduced from  $\sim 15$  to  $\sim 10$  ppm.

From the results in Sect. 3.1.1, 3.1.2, and 3.1.3, we observe that CO<sub>2</sub> profile retrievals do not need accurate prior knowledge of the CO<sub>2</sub> profile but require accurate knowledge of the prior temperature and water vapor profiles. Moreover, these results suggest that errors in the temperature profile are the main source of deviations from the truth in retrieved CO<sub>2</sub> profiles. Retrievals using the two Weak windows are the least affected by biases in the prior temperature and water vapor profiles. The need for accurate a priori water vapor profile could be alleviated by retrieving H<sub>2</sub>O profiles simultaneously with CO<sub>2</sub> profiles, but this was not tested with GFIT2, which currently can only retrieve the main target gas in a window with profile retrievals. In addition, H<sub>2</sub>O profile retrievals would also be affected by temperature errors.

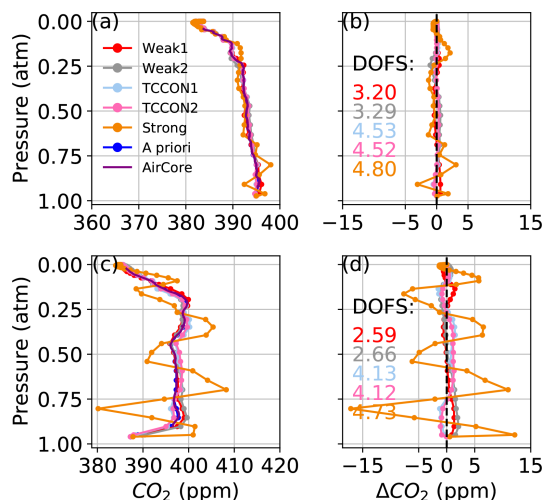


**Figure 5.** The left-hand panels show CO<sub>2</sub> profiles retrieved using synthetic spectra. 10 % is added to the H<sub>2</sub>O profile below 5 km for (a) dry conditions on 14 January 2012 and for (c) wet conditions on 23 July 2013. Panels (b) and (d) show the difference between the retrieved profiles and AirCore, corresponding to (a) and (c) respectively.

### 3.1.4 Perturbed line parameters

The line list used by GGG is a compilation of different versions of the HITRAN line lists (Gordon et al., 2017; Rothman et al., 2005, 2009, 2013; Toon, 2015; Toon et al., 2016). GGG2020 has the option to use either the qSDV+LM line shape or the Voigt line shape for some windows and gases (Mendonca et al., 2016, 2017, 2019). The reference line lists and the uncertainties on air- and self-broadened Lorentz half-width coefficients, as well as their temperature dependence, are summarized in Table 4. The qSDV+LM line shape is only implemented for the CO<sub>2</sub> lines of the two TCCON windows and the Strong window, for the CH<sub>4</sub> lines of the Weak1 window, and for the O<sub>2</sub> lines of the oxygen window centered at 7885 cm<sup>-1</sup>. The qSDV+LM line shape is not implemented for the CO<sub>2</sub> lines of the Weak1 and Weak2 windows, but these weak lines are minimally affected by line mixing, and they lack laboratory measurements of speed-dependent line parameters. The effect of errors in the half-width coefficients on the retrieved CO<sub>2</sub> profiles was tested by increasing both the self- and air-broadened Lorentz half-width coefficients by 0.1 % for all CO<sub>2</sub> lines as shown in Fig. 7a. This perturbation corresponds to the median uncertainty of these parameters in the Strong and TCCON windows as shown in Table 4. This caused deviations of up to 10 ppm in the Strong window, 5 ppm in the TCCON windows, and 2 ppm in the Weak windows. Similar deviations are obtained by perturbing the temperature dependence of the half-width coefficients by  $-1$  % as shown in Fig. 7b. In this case, the deviations appear symmetric with the a priori profile compared to Fig. 7a. The shape of deviations in both cases is similar; it is also

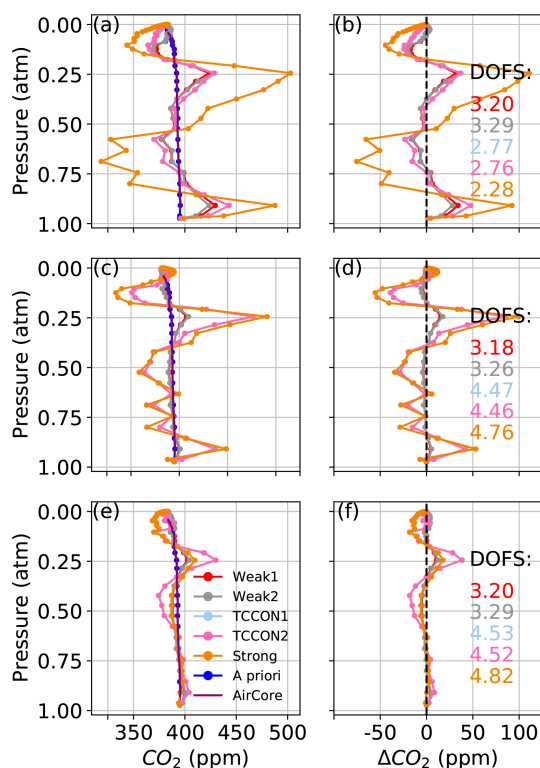


**Figure 6.** The left-hand panels show CO<sub>2</sub> profiles retrieved using synthetic spectra for (a) +5 °C added to the a priori temperature profile below 5 km, (c) +2 °C between 8 and 13 km, and (e) +2 °C above 15 km. Panels (b), (d), and (f) show the difference between the retrieved profiles and AirCore profile, corresponding to (a), (c), and (e) respectively. Note the difference in the horizontal axis range between the panels. Here 5 km corresponds to ~0.55 atm, 8–13 km to ~0.36–0.17 atm and 15 km to ~0.125 atm.

similar to the shape obtained in Fig. 6 from perturbing the temperature profiles. This is because all those perturbations ultimately lead to an altered line width and all cause residuals patterns that cannot be distinguished from each other, as illustrated in Fig. 8. This implies that errors in the a priori temperature profile, water vapor profile, and spectroscopic widths are difficult to disentangle in the current GFIT2 profile retrieval. A simultaneous temperature (hence pressure) and CO<sub>2</sub> profile retrieval would be necessary to overcome these issues.

A factor of 10 increase in the perturbations applied to the width coefficients or their temperature dependence also leads to a factor of 10 increase in the amplitude of deviations in the retrieved CO<sub>2</sub> profiles. Figure 7a and b use perturbations corresponding to uncertainties in the line parameters when using qSDV+LM for the TCCON windows and the Strong window. The same perturbations were applied for all five windows. However, in the Weak1 and Weak2 windows, these perturbations are 10 times smaller than realistic uncertainties as reported in Table 4 for the Voigt line shape. Therefore, for

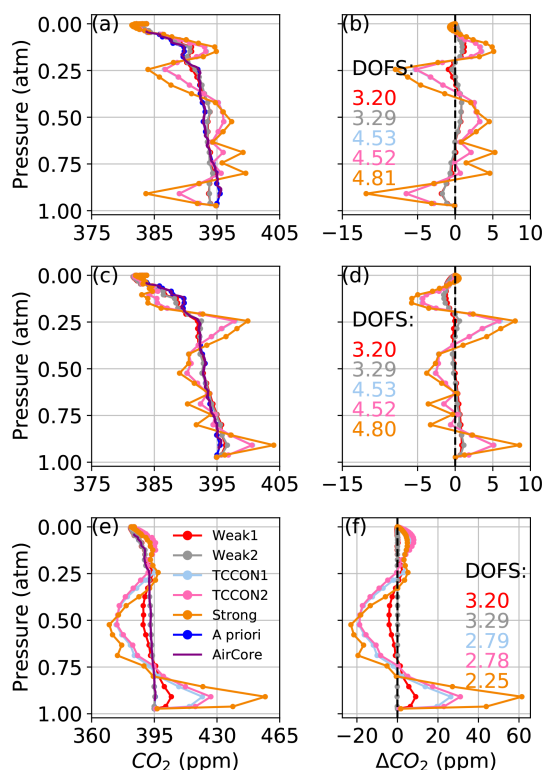


**Figure 7.** The left-hand panels show CO<sub>2</sub> profiles retrieved using synthetic spectra. In (a) the air- and self-broadened half-width coefficients of all CO<sub>2</sub> lines is increased by 0.1 %. In (c) the temperature dependence of these coefficients is decreased by 1 %. In (e), the synthetic spectrum used as “measurement” is generated with the speed-dependent Voigt line shape with line mixing, but profiles are retrieved using a Voigt line shape. Panels (b), (d), and (f) show the difference between the retrieved profiles and AirCore, corresponding to (a), (c), and (e) respectively.

the Weak windows, we can expect deviations from the truth 10 times larger than in Fig. 7, within ~10–20 ppm.

In Connor et al. (2016), the authors used a Voigt line shape. Figure 7e shows the effect of fitting with a Voigt line shape a synthetic spectrum that was generated using qSDV+LM. In that case the fit residuals in the Strong window can exceed 1 % and the residuals in the TCCON windows can exceed 0.5 %. For these retrievals, the SNR is set to 100 in the Strong window, 200 in the TCCON windows, and 1000 in the Weak windows. The profiles retrieved from the Strong window present deviations from the truth within 60 ppm. In the two TCCON windows, the deviations from the truth are within 30 ppm. In the Weak1 window, the deviations from the truth are within 10 ppm, because qSDV+LM was not used to calculate the CO<sub>2</sub> line absorptions themselves, but only for the relatively strong CH<sub>4</sub> lines in that window. In the Weak2 window, there is no difference between the two line lists or line shape, and thus the retrieved profile does not differ from the a priori profile. Therefore, even if we assume perfect a priori meteorology, the deviations in the CO<sub>2</sub> profiles re-

**Table 4.** The  $1\sigma$  relative errors of the air- and self-broadened Lorentz half-width coefficients ( $b$ ) and of their temperature dependence ( $n$ ). The values from Benner et al. (2016) and Devi et al. (2007a, b) use the median  $1\sigma$  uncertainty for the whole band, from the Appendix or supplemental files of these studies. The values for the Voigt line shape use the error codes reported in the HITRAN2016 line list (Gordon et al., 2017).

Line shape	Window (band)	$b$ (air) (%)	$n$ (air) (%)	$b$ (self) (%)	$n$ (self) (%)	Reference
Voigt	TCCON1		–			Toth et al. (2008)
	TCCON2	$\geq 1$ and $< 2$		$\geq 1$ and $< 2$		
	Weak1		From $< 10$			– Lamouroux et al. (2015),
	Weak2		to $< 1$			Gordon et al. (2017)
	Strong					
qSDV+LM	TCCON1 (30013–00001)	0.13	–	0.07		Devi et al. (2007a)
	TCCON2 (30012–00001)	0.14		0.07		Devi et al. (2007b)
	Strong (20013–00001)	0.03	0.12	0.09	0.33	Benner et al. (2016)
	Strong (21113–01101)	0.25	1.47	0.49	2.27	

trieved from the TCCON1 window observed by Connor et al. (2016) when fitting real spectra could be entirely due to the use of the Voigt line shape.

The effect of the errors in the a priori water vapor and temperature profiles and in the spectroscopic parameters cannot be mitigated by adjusting the measurement covariance, for example by using a variable SNR. Figure 8 shows an example of spectral residuals from fits to synthetic spectra from the Strong window using scaling retrievals, but with different perturbations applied. Showing residuals from scaling retrievals reveals systematic features that the profile retrieval will attempt to suppress. Figure 8b presents residuals from fitting a synthetic spectrum using the same a priori profile that was used to generate the synthetic spectrum. It shows small ( $< 0.05\%$ ) residuals, caused by the use of a constant ILS across the window for a faster convolution of the spectrum with the ILS. The corresponding profiles are shown in Fig. 4a. In Fig. 8c, a  $2^\circ\text{C}$  offset is applied to the a priori temperature profile between 8 and 13 km before fitting the synthetic spectrum. In Fig. 8d, a constant a priori CO<sub>2</sub> profile is used to fit a synthetic spectrum that was generated with an AirCore CO<sub>2</sub> profile as an a priori profile. In Fig. 8e, the air- and self-broadened Lorentz half-width coefficients are increased by  $0.1\%$  compared to the parameters used to generate the synthetic spectrum. In Fig. 8f, the temperature dependence of the air- and self-broadened Lorentz half-width coefficients is decreased by  $1\%$  compared to the parameters used to generate the synthetic spectrum. In Fig. 8g, the GGG2020 a priori meteorology and trace gas profiles are used as a priori profiles instead of the a priori profiles constructed with AirCore profiles used to generate the synthetic spectrum.

In all panels of Fig. 8 except panels (c) and (g), all the residual features correspond to CO<sub>2</sub> absorption lines. In Fig. 8c, with a perturbation to the a priori temperature profile, there is an added contribution of temperature errors on interfering species. Furthermore, the residuals in Fig. 8g result from a combination of errors in the a priori meteorology and trace gas profiles but are dominated by temperature errors. Perturbations in the temperature profile, CO<sub>2</sub> profile, or CO<sub>2</sub> line width coefficients all cause residuals with the same shape because they all affect the width of CO<sub>2</sub> lines. It is not possible to de-weight the effect of any of those errors by adjusting the measurement error without also losing the ability to correct for residuals caused by CO<sub>2</sub> errors. Residuals caused by realistic temperature errors as shown in Fig. 8c are of the same magnitude as those caused by unrealistically high errors in the a priori CO<sub>2</sub> profile shape as shown in Fig. 8d.

### 3.1.5 Synthetic spectra: discussion

For retrievals on synthetic spectra, the “measurement” SNR is set to 1000, which is high compared to most solar spectra measured by TCCON. So in profiles retrieved from real spectra, we can expect a greater influence of the a priori CO<sub>2</sub> profile: the deviations will be smaller, and the degrees of freedom for signal will be lower than those shown in the figures of Sect. 3.1. This is not a desirable outcome; the a priori CO<sub>2</sub> covariance is meant to nudge the retrieval such that the solution lies close to realistic ensembles of CO<sub>2</sub> profiles, not to constrain deviations caused by temperature errors. Tuning the a priori or measurement covariances is not the right approach until profile deviations caused by typical errors in spectroscopy or meteorology are smaller than typical vertical variations in CO<sub>2</sub> profiles. Figure 4 shows that the profile retrieval algorithm works well and could be a powerful tool

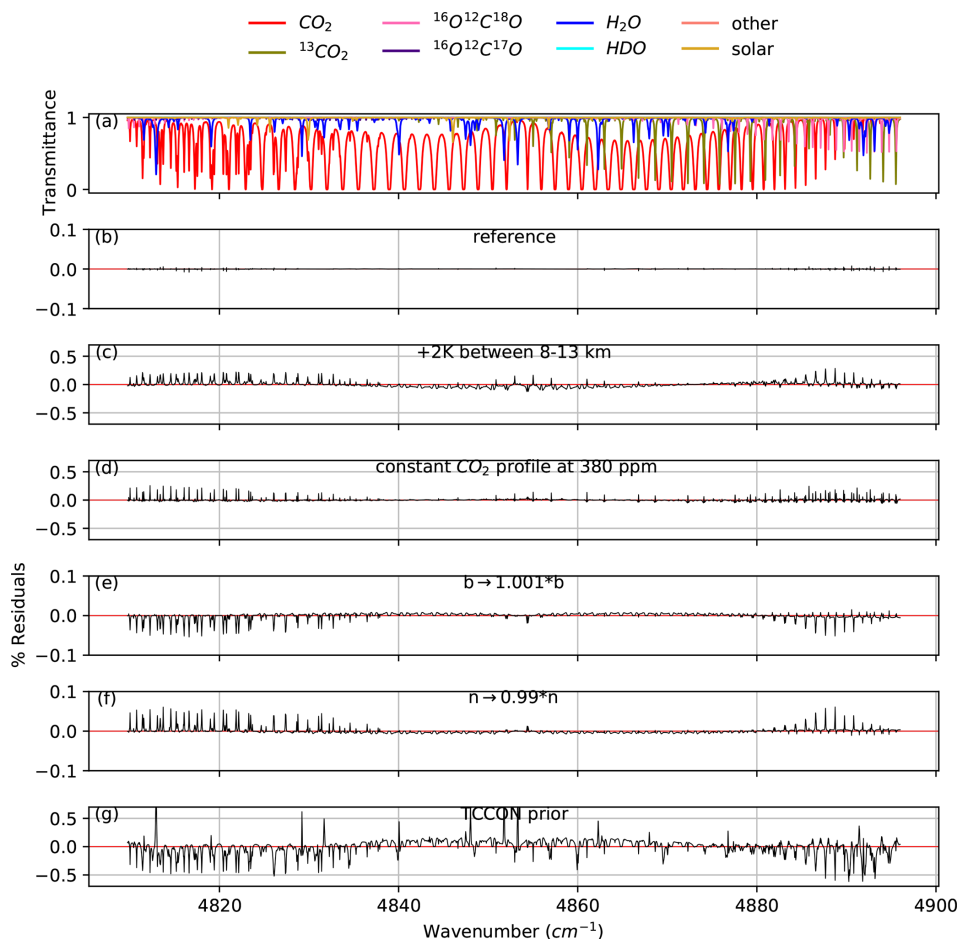


**Figure 8.** Panel (a) shows an example of calculated lines in the Strong CO<sub>2</sub> window. The other panels show residuals from fits to a synthetic spectrum, using the same inputs used to generate the synthetic spectrum except for (b) no perturbation; (c) +2 °C perturbation to the a priori temperature between 8 and 13 km; (d) a CO<sub>2</sub> prior profile set to 380 ppm at all levels, corresponding to ~ 15 ppm offset from the unperturbed prior; (e) air- and self-broadened Lorentz half-width coefficients increased by 0.1 %; (f) temperature dependence of the half-width coefficients decreased by 1 %; and (g) using the a priori profiles that would be used by TCCON operational processing, instead of that constructed from in situ measurements, resulting in a combination of different errors in the a priori profiles such as H<sub>2</sub>O, temperature, and CO<sub>2</sub>. Note the vertical scale of panels (b), (e), and (f) is 5 times smaller than that of panels (c), (d), and (g).

to derive information about the vertical distribution of CO<sub>2</sub>, even with ill-defined a priori CO<sub>2</sub> profiles. Panels (a) and (b) of Fig. 7 show that profile information could still be retrieved to within ~ 5 ppm given realistic errors in line width parameters. But as shown with Fig. 6, a temperature retrieval, or correction, is critical to producing reliable CO<sub>2</sub> profile retrievals. This study does not show the effect of typical instrument misalignment errors on the retrieved profiles. GFIT2 currently has no capacity to fit the instrument line shape (ILS) of a misaligned instrument given specific angular and shear misalignments and instead always assumes a perfect ILS. This is an area of future development for the program. The effect of an error in the instrument's internal field of view and the effect of a zero-level offset are presented in Appendix F; both should lead to minor deviations from the truth, within less than 3 ppm.

In Sect. 3.2, GFIT2 is tested with real spectra using a priori profile built from in situ measurements. In that case, the deviations from the truth in the retrieved CO<sub>2</sub> profile caused by errors in the a priori meteorology (temperature, pressure, and water vapor profiles) are minimized, and the remaining deviations are caused by errors in the spectroscopic line parameters, in the radiative transfer, in the instrument line shape, or in the pointing of the sun tracker.

### 3.2 Real spectra

Here the algorithm is tested with real spectra measured at Lamont as described in Sect. 2.2. A scaling retrieval is performed before each profile retrieval and the root mean square of the residuals from the scaling retrieval is used as measurement uncertainty for the profile retrieval. Since the residuals from the scaling retrieval include systematic features larger

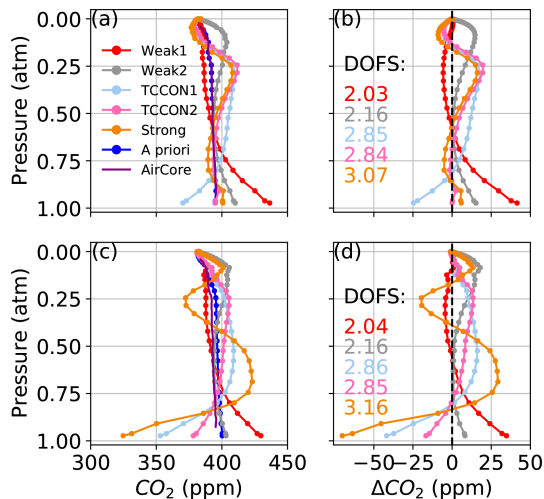


**Figure 9.** CO<sub>2</sub> profiles retrieved from spectra measured at the Lamont TCCON site on 14 January 2012, at 61–74° solar zenith angle, coincident with AirCore measurements using (a) the AirCore “truth” as a priori profiles and (c) the GGG2020 a priori profiles. In (b) and (d) the difference of the retrieved profiles minus the AirCore profile is shown, corresponding to (a) and (c), respectively. The points represent the 51 levels of the vertical grid. The DOFs for each retrieval window are indicated in (b) and (d).

than the random noise in the measurement, the root mean square is a conservative estimate of the noise. In Sect. 3.2.1, we present CO<sub>2</sub> profiles retrieved from real spectra and we attempt to isolate the effect of errors in instrument line shape, in spectroscopic parameters, and in pointing, from the effect of errors in meteorology. In Sect. 3.2.2, we present an analysis of the information content and altitude sensitivity of the retrieval. Finally, in Sect. 3.2.3, we compare XCO<sub>2</sub> derived from the scaling retrieval to XCO<sub>2</sub> derived from the profile retrieval.

### 3.2.1 Profiles

Figures 9 and 10 show CO<sub>2</sub> profiles retrieved from real spectra measured from Lamont, OK, on 14 January 2012 and 11 April 2017, respectively. In each figure, panel (a) shows profiles retrieved using in situ profiles (the “truth”) as the a priori profiles. In those cases, we assume that deviations from the truth caused by errors in a priori meteorology (pressure, temperature, and water vapor profiles) are minimized, and the remaining deviations can be attributed to the combination of instrument misalignment (ILS), pointing errors, or errors in spectroscopic parameters. Panel (c) shows profiles retrieved using the GGG2020 a priori profiles. A first complication for obtaining a satisfactory CO<sub>2</sub> profile retrieval is that the a priori CO<sub>2</sub> profiles in GGG2020 already compare well with in situ profiles, typically within 5 ppm over Lamont. In Figs. 9c and 10c, the profile that most closely matches the AirCore is the a priori profile.

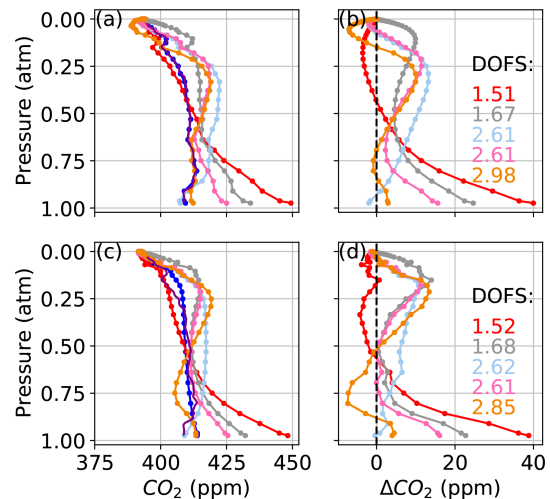


**Figure 10.** Same as Fig. 9 but for spectra measured on 11 April 2017 at 28–39° solar zenith angle.

Even with ideal prior knowledge of the meteorology and trace gas profiles, the CO<sub>2</sub> deviations from the truth can be as large as 50 ppm as shown in Figs. 9a and 10a. When synthetic spectra were perturbed with realistic errors in line width parameters, profile deviations remained within 5 ppm for profiles retrieved from the Strong window and within 10 ppm for the TCCON windows. This suggests that the main cause of deviations in Figs. 9a and 10a is not due to errors in spectroscopic parameters. The assumption that there is no contribution from temperature errors in the radiosonde profile is supported by the CO<sub>2</sub> profile deviation being smallest in the Strong window, which is the most sensitive to temperature errors. Although the effect of typical perturbations in the instrument field of view, zero-level offset, and spectroscopic parameters is relatively small compared to the effect of temperature errors, the cumulative effect of these errors could explain the deviations from the truth in Figs. 9a and 10a.

Figure 11 shows the difference between the GGG2020 a priori temperature profile, used in Figs. 9c and 10c, and the radiosonde temperature profile used in Figs. 9a and 10a. In both cases, we replace the a priori surface temperature with the measured surface temperature. On 14 January 2012, the radiosonde temperature profile is about 1 °C higher than the GGG2020 a priori profile at pressures < 0.6 atm. The shape of the Strong window CO<sub>2</sub> profile deviations in Fig. 9c is consistent with the sensitivity tests using synthetic spectra in Sect. 3.1.3. In Fig. 6a, a +5 °C offset below 5 km results in +500 ppm CO<sub>2</sub> error at ~0.9 atm, while in Fig. 10, a –1 °C offset in the lower troposphere leads to a –50 ppm error at ~0.9 atm. The deviations are smoother in Figs. 9 and 10 than in Fig. 6 because the SNR of real spectra is between 200 and 500 instead of 1000, and because of the smoothing effect of the off-diagonal elements of the a priori covariance used in this section. The off-diagonal elements of

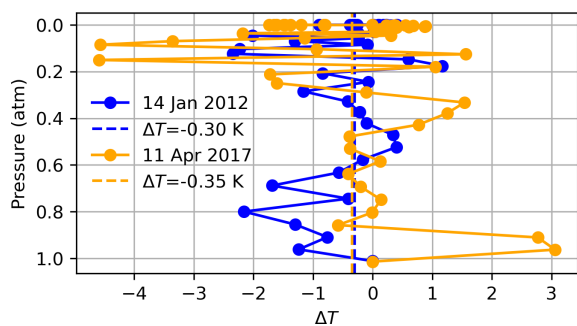


**Figure 11.** Temperature profile difference for the GGG2020 a priori minus radiosonde on 14 January 2012 and 11 April 2017. The radiosonde profile is included in the a priori profiles used in panel (a) of Figs. 9 and 10, and the GGG2020 a priori profiles are used in panel (b) of Figs. 9 and 10. In situ temperature measurements are used for both cases at the surface. The dashed line marks the average difference, with the value indicated in the legend.

the a priori covariance introduce inter-layer correlations that reduce large differences between levels over a given length scale (see Sect. 2.2). Retrievals on real spectra after applying a  $+5^{\circ}\text{C}$  offset to the radiosonde temperature profile below 5 km lead to a  $+100$  ppm offset at  $\sim 0.9$  atm. The CO<sub>2</sub> profiles in Fig. 10c differ less with those in Fig. 10a than do the profiles in Fig. 9a and c. In Fig. 11, the difference between the GGG2020 and radiosonde temperature profile on 11 April 2017 is  $\sim 3^{\circ}\text{C}$  for the first two levels above the surface, but the average difference between 0.85 and 0.6 atm is  $-0.15^{\circ}\text{C}$  compared to  $-1.05^{\circ}\text{C}$  on 14 January 2012.

In aircraft profiles over Lamont between 2008 and 2018 from NOAA's ObsPack, the steepest vertical gradients in CO<sub>2</sub> profiles are  $\sim 5$  ppm km<sup>-1</sup> between the surface and  $\sim 3$  km. In its current state, CO<sub>2</sub> profile retrieval with GFIT2 cannot distinguish these vertical variations from CO<sub>2</sub> deviations caused by errors in the forward model, even with very accurate a priori meteorology. Typical errors in the a priori temperature profiles will prevent operational use of CO<sub>2</sub> profile retrieval without a scheme for retrieving or correcting the temperature profiles.

### 3.2.2 Information content and averaging kernel

Table 5 presents the average values of the Shannon information content,  $H$ , and of the CO<sub>2</sub> profile DOFs, from all profile retrievals performed on Lamont spectra when using the GGG2020 a priori profiles. It also includes the ratio of residuals (RR) of the spectral fits (see Appendix B, Eq. B10), which represents the residuals of the profile retrievals as a fraction of the residuals of the scaling retrievals. The same quantities are plotted in Fig. 12 for each spectrum. The RR is always smaller than 1 because the profile retrieval has more freedom to adjust the calculated spectrum and so can never produce larger residuals than scaling retrievals. Figure 12 also shows XCO<sub>2</sub> obtained from the scaling retrievals

**Table 5.** Shannon information content ( $H$ ), degrees of freedom for signal (DOFs) for the CO<sub>2</sub> profile, and ratio of residuals (RR) averaged over all 492 profile retrievals from near-infrared TCCON spectra measured at Lamont and coincident within  $\pm 1$  h of the AirCore last sampling time. The standard deviation is also shown.

Window name	$H$	DOFs	RR
TCCON1	$5.4 \pm 0.6$	$2.7 \pm 0.2$	$0.988 \pm 0.014$
TCCON2	$5.4 \pm 0.6$	$2.7 \pm 0.2$	$0.992 \pm 0.009$
Weak1	$2.3 \pm 0.7$	$1.7 \pm 0.3$	$0.996 \pm 0.002$
Weak2	$2.5 \pm 0.9$	$1.8 \pm 0.4$	$0.994 \pm 0.008$
Strong	$6.8 \pm 1.0$	$3.0 \pm 0.4$	$0.957 \pm 0.038$

subtracted to XCO<sub>2</sub> obtained from profile retrievals for each window.

Figure 13 shows the sums of the rows of the partial column averaging kernel matrix over different altitude ranges. The sum from 0 to 70 km is the total column averaging kernel (see Appendix C). The total column averaging kernel is close to 1 at all levels in all windows, indicating good sensitivity to changes in the CO<sub>2</sub> total column. The partial column kernels show that most of this sensitivity comes from altitudes below 15 km. That the total column averaging kernel is close to 1 at all levels is not inconsistent with the large deviations we observe in the retrieved CO<sub>2</sub> profiles. If the total column averaging kernel is exactly one at each level, adding  $N$  molecules of CO<sub>2</sub> anywhere in the atmosphere will lead to  $N$  more molecules in the retrieved total column. However, in the presence of a priori temperature errors, for example, the retrieved value can be biased. The averaging kernel indicates that without the effect of these errors, the CO<sub>2</sub> profile retrieval would have excellent sensitivity to CO<sub>2</sub> and would be able to provide information about CO<sub>2</sub> in two distinct layers. Here, the vertical representation is not a concern. Using 51 vertical levels only affects the speed of the retrieval. The retrieved profiles can then be reduced to a number of partial columns corresponding to the DOFs. This was not done here because it is evident that large deviations due to temperature errors could easily bias the resulting partial columns. The reduction into a subset of layers also requires an arbitrary choice: in Fig. 13 the altitude ranges were set such that the DOFs of the first two partial columns would be roughly close to 1 in each window. We could also have chosen two regions with approximately equal DOFs from 0–7 and 7–70 km. The partial column averaging kernels overlap with each other, so the partial columns are not completely uncorrelated even if their respective DOFs are higher than 1. The DOFs are not exactly independent pieces of information, as it is impossible to obtain independent partial column amounts from direct-sun measurements on the ground (see Appendix C), but an arbitrary criterion can be defined to identify distinct layers, for example if the peaks in their partial column averaging kernels are separated by a given fraction of their widths in altitude.

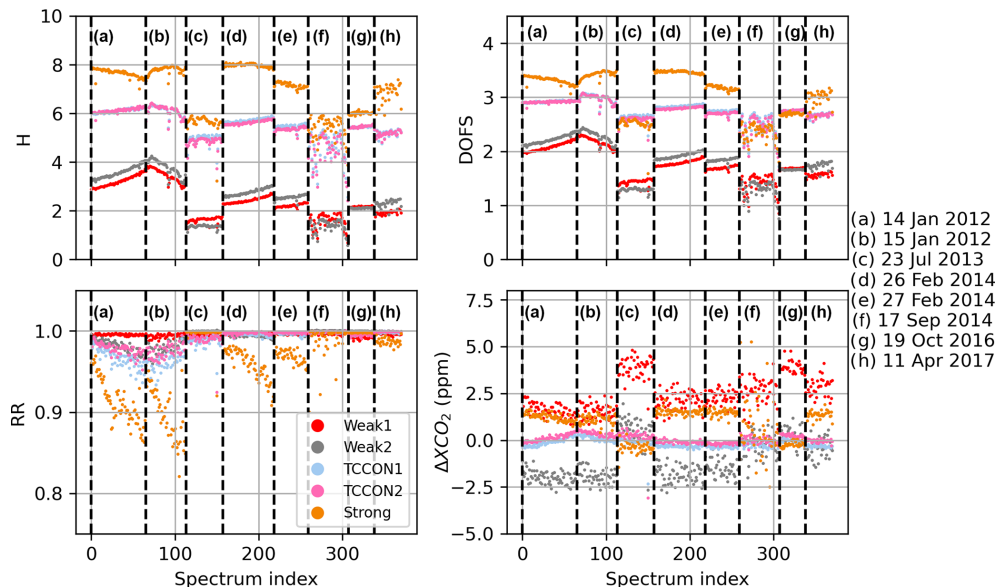


**Figure 12.** Shannon information content (top left), degrees of freedom for signal for the CO<sub>2</sub> profile (top right), and ratio of residuals (bottom left), and profile minus scaling retrieval XCO<sub>2</sub> (bottom right) for all Lamont spectra coincident within  $\pm 1$  h of the AirCore last sampling time for AirCores launched on the dates indicated on the right. Each new date is marked by a vertical dashed line.

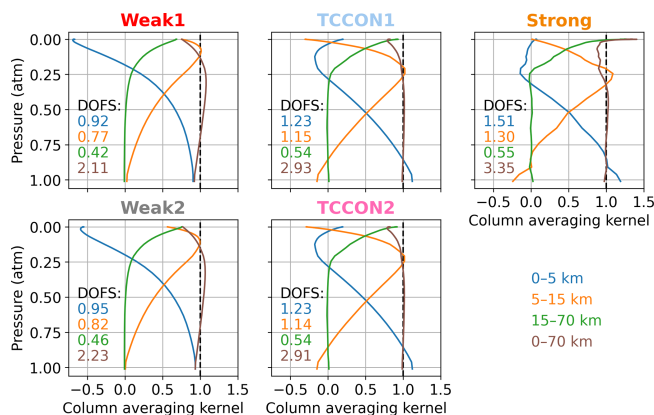


**Figure 13.** Sum of the rows of the partial column averaging kernel matrix over different altitude ranges as indicated by the legend, for each of the five CO<sub>2</sub> windows. The sum between 0–70 km is the total column averaging kernel. The numbers in each panel are the DOFs corresponding to each of the altitude ranges.

Additional analysis of the vertical sensitivity of the retrieval is presented in Appendix D, as well as a decomposition of the retrieval error into the interference, measurement noise, and smoothing errors as shown in Fig. D8. The interference error is the smallest ( $< 0.5\%$ ) contribution but does not include the effect of temperature errors. The measurement noise error decreases from  $\sim 1\%$  at the surface to  $\sim 0.2\%$  at pressures less than 0.6 atm ( $> 5$  km), and the smoothing error dominates and decreases roughly from  $\sim 3\%$  at the surface to  $1\%$  at the top of the atmosphere.

### 3.2.3 XCO<sub>2</sub>

The XCO<sub>2</sub> derived from profile and scaling retrievals using the GGG2020 a priori profiles was compared to XCO<sub>2</sub> derived from the CO<sub>2</sub> profile built from the AirCore CO<sub>2</sub> profile, in situ surface measurements of CO<sub>2</sub>, and the GGG2020 a priori CO<sub>2</sub> above the maximum altitude sampled by the AirCore. The results are shown in Fig. 14 for the 8 days we have AirCore profiles that are coincident with measurements at the Lamont TCCON station. Despite the large deviations observed in retrieved profiles, the XCO<sub>2</sub> derived from profile retrievals compares well to the AirCore XCO<sub>2</sub>, but it does not present a clear improvement over the XCO<sub>2</sub> derived from the scaling retrievals. The effect of temperature errors on XCO<sub>2</sub> derived from scaling and profile retrievals is relatively small because the spectral windows utilize the entire (fundamental) band. Across a wide window, the residuals due to temperature errors show alternating positive and negative residuals, because of the different temperature sensitivities of absorption lines. Collectively, these lines have a small net temperature sensitivity. The scaling retrieval, which can only add or remove CO<sub>2</sub> at all levels simultaneously, is limited in its ability to fit out such residuals across a wide window by adjusting the CO<sub>2</sub> scale factor. For profile retrievals, although large deviations are observed in the retrieved profile, they compensate each other when deriving the total column. These deviations compensate due to the wide windows including a range of spectral lines with different temperature sensitivities. If a narrow window over only a few lines were used instead, we would expect more localized errors in the retrieved CO<sub>2</sub> profiles, and total columns sensitive to temperature errors.

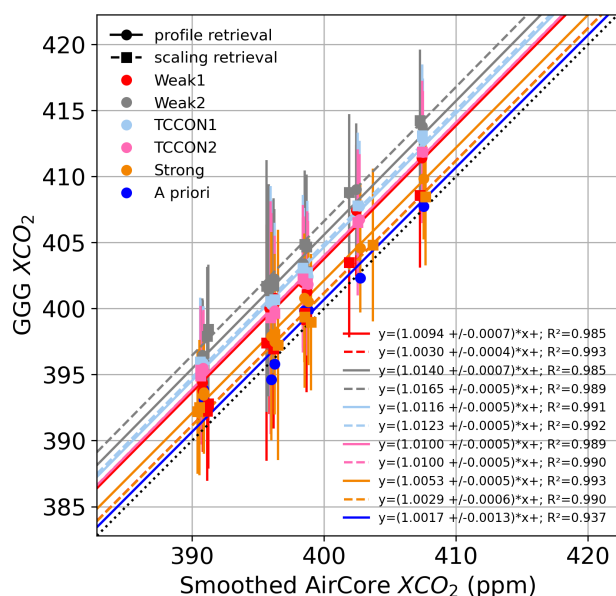


**Figure 14.** XCO<sub>2</sub> derived from scaling (dashed lines and squares) and profile (solid lines and circles) retrievals for each CO<sub>2</sub> window when using the GGG2020 a priori profiles, compared to XCO<sub>2</sub> derived from smoothed AirCore profiles (see Appendix C). The black dotted line marks the 1-to-1 line. When comparing with scaling retrievals, the AirCore profile is smoothed using the total column averaging kernel of the scaling retrieval, and when comparing to profile retrievals the AirCore profile is smoothed using the averaging kernel matrix of the profile retrieval. The legend indicates the slopes and squared Pearson correlation coefficients of fits to lines passing through the origin, assuming that in the absence of CO<sub>2</sub> the retrieval would return a CO<sub>2</sub> value of zero.

### 3.2.4 Real spectra: discussion

Profile retrievals that use real spectra and an a priori profile built from coincident in situ measurements show CO<sub>2</sub> profile deviations up to 40–50 ppm. Even when the errors due to the a priori meteorology are minimized, deviations from the truth due to instrument misalignment, radiative transfer, sun-tracker pointing, or uncertainties in line parameters are larger than the steepest vertical CO<sub>2</sub> gradients ( $\sim 5 \text{ ppm km}^{-1}$ ) observed in the ensemble of aircraft profiles from NOAA's ObsPack.

When performing retrievals on the same spectra but replacing the AirCore a priori profile with a standard a priori profile, small errors in the a priori temperature profile cause large deviations in the retrieved CO<sub>2</sub> profile. Despite the large deviations in the retrieved profiles, the retrieval still shows high sensitivity to XCO<sub>2</sub> but does not present a clear improvement over XCO<sub>2</sub> obtained from scaling retrievals. Introducing a temperature retrieval or correction, as well as the ability to model an imperfect instrument line shape, is the best avenue to improve the CO<sub>2</sub> profile retrieval results. Appendix E presents an attempt at applying empirical cor-

rections to reduce the effect of systematic imperfections in the forward model.

## 4 Summary and conclusions

In this study we investigated the use of CO<sub>2</sub> profile retrievals from near-infrared solar absorption spectra measured by TCCON. The performance of CO<sub>2</sub> profile retrieval was reassessed after improvements were implemented in the forward model of GGG. Retrievals were performed using five CO<sub>2</sub> windows with significantly different optical opacities.

We first use retrievals on synthetic spectra to check the self-consistency. Typical errors in the a priori H<sub>2</sub>O profile, which is retrieved with a scaling retrieval, caused limited deviations from the truth in the CO<sub>2</sub> profile, within 5–10 ppm in the Strong window, and within 2 ppm in the other windows. Perturbing the CO<sub>2</sub> air- and self-broadened Lorentz half-width coefficients and their temperature dependence to within their estimated uncertainties led to CO<sub>2</sub> deviations from the truth of less than 5 ppm. The implementation of a non-Voigt line shape is a significant improvement to CO<sub>2</sub> profile retrievals; errors in spectroscopic parameters are no longer the leading source of uncertainty in retrieved profiles. We observed deviations from the truth of up to 100 ppm in profiles retrieved with typical temperature errors. The temperature profile is an important retrieval input but is not retrieved; thus spectral residuals caused by errors in the a priori temperature profile are free to be suppressed by adjustments to the CO<sub>2</sub> scale factors. The implementation of a temperature profile retrieval, or correction, is critical to improve CO<sub>2</sub> profile retrieval results. In GGG2020, 3-hourly a priori temperature profiles are used, but temperatures can still vary by several degrees between 3-hourly profiles and can still be wrong even without any time mismatch. Temperature could be retrieved from CO<sub>2</sub> windows and from windows with temperature-sensitive water vapor absorption lines.

We then perform retrievals with atmospheric TCCON spectra collected at the Lamont site, which were coincident with AirCore profiles, including radiosonde profiles of temperature and relative humidity; these were considered as the true state of the atmosphere. When running retrievals with the truth as the a priori profiles, the deviations due to errors in the a priori meteorology are minimized and the resulting deviations are caused by instrument misalignment, errors in spectroscopy, or sun tracker pointing. We observed CO<sub>2</sub> deviations of up to 40 ppm in that case. Even with ideal knowledge of the a priori meteorology, the CO<sub>2</sub> deviations are larger than the largest expected vertical CO<sub>2</sub> variations and no useful profile information can be inferred from the profile retrieval. Stricter alignment requirements, which can be challenging to achieve in practice, or the ability to model an imperfect instrument line shape are needed to improve profile retrieval results. The sensitivity study of Sect. 3.1 could then

be extended to assess the effect of specific misalignments on the retrieved profiles.

In these retrievals, we used a full a priori covariance matrix, with off-diagonal elements, based on comparisons between the GGG2020 a priori and aircraft vertical profiles from NOAA's ObsPack over the Lamont TCCON site. Before tuning the a priori covariance and considering stronger regularizations, it must be shown that CO<sub>2</sub> deviations caused by typical errors in the a priori meteorology are smaller than typical variability in real CO<sub>2</sub> profiles. Because it is more computationally expensive, and because it requires stronger constraints on the a priori statistics than scaling retrievals, a profile retrieval must present clear advantages over a scaling retrieval to justify its operational use. And with each new improvement to the CO<sub>2</sub> a priori profiles, requirements for profile retrieval to be better than scaling retrieval become more stringent.

A method to combine the profiles obtained from sequential retrievals in different spectral windows still needs to be developed. Alternatively, the ability to perform simultaneous retrievals using multiple spectral windows could be implemented in GFIT2.

## Appendix A: Vertical columns

The vertical grid for the retrievals presented in this study has 51 levels from 0 to 70 km, with spacing increasing with altitude and following:

$$z_i = i \times (0.4 + 0.02 \times i), \quad (\text{A1})$$

where  $z_i$  is the altitude in kilometers of the  $i$ th level. Each level is associated with an effective vertical path distance  $vp$ :

$$vp_i \approx 0.4 + 0.04 \times i. \quad (\text{A2})$$

The total column of air in molecules per square meter can be obtained as

$$\text{column}_{\text{Air}} = \sum_{i=1}^N vp_i \times d_i, \quad (\text{A3})$$

where  $d$  is the air number density in molecules of air per cubic meter.  $N$  is the number of atmospheric levels. If the prescribed grid contains layers below the altitude of the site considered, their effective vertical path will be 0. The layer containing the site altitude will be truncated. The total column of CO<sub>2</sub> is

$$\text{column}_{\text{CO}_2} = \sum_{i=1}^N sf_i \times \text{vmr}_i \times d_i \times vp_i, \quad (\text{A4})$$

where  $sf$  is the retrieved scaling factor and  $\text{vmr}$  is the a priori CO<sub>2</sub> wet mole fraction (molecules of CO<sub>2</sub> per molecules of air). In the forward model, the retrieval grid is not vertical, but along the slant path from the instrument towards the sun, the scaling factors retrieved for the slant layers are used with the corresponding vertical layers to compute the vertical column. The a priori profiles used by GFIT are built on the prescribed altitude grid directly above the site. This should contribute to an unknown error, largest at high solar zenith angles when the projection of the sun ray on the ground can reach a few hundred kilometers; in that case the a priori slant profiles of temperature and H<sub>2</sub>O could be significantly different from the vertical profile directly above the instrument.

The column-averaged dry-air mole fraction of CO<sub>2</sub> ( $X_{\text{CO}_2}$ ) is the ratio of the column of CO<sub>2</sub> to the column of dry air, where the column of dry air is expressed as the column of O<sub>2</sub> divided by 0.2095 (Wunch et al., 2011b):

$$X_{\text{CO}_2} = 0.2095 \times \frac{\text{column}_{\text{CO}_2}}{\text{column}_{\text{O}_2}}, \quad (\text{A5})$$

where the O<sub>2</sub> column is retrieved from a spectral window centered at 7885 cm<sup>-1</sup>. For the official TCCON products,  $\text{column}_{\text{CO}_2}$  is a weighted average of the columns retrieved from the TCCON1 and TCCON2 windows.

## Appendix B: GFIT2 algorithm

To find the state vector with maximum a posteriori probability given a measurement, the cost function  $J$  is minimized,

$$J = (\mathbf{y} - f(\mathbf{x}))^T \mathbf{S}_y^{-1} (\mathbf{y} - f(\mathbf{x})) + (\mathbf{x}_a - \mathbf{x})^T \mathbf{R} (\mathbf{x}_a - \mathbf{x}), \quad (\text{B1})$$

by iteratively solving for the state update  $\Delta \mathbf{x}$  in the least square problem:

$$\left( \mathbf{K}_i^T \mathbf{S}_y^{-1} \mathbf{K}_i + \mathbf{R} + \gamma \mathbf{D} \right) \Delta \mathbf{x} = \mathbf{K}_i^T \mathbf{S}_y^{-1} (\mathbf{y} - f(\mathbf{x}_i)) + \mathbf{R} (\mathbf{x}_a - \mathbf{x}_i). \quad (\text{B2})$$

Here,  $\mathbf{y}$  is the measured transmittance spectrum,  $f$  is the forward model that computes a transmittance spectrum from the state vector  $\mathbf{x}$ ,  $\mathbf{S}_y$  is the measurement covariance matrix,  $\mathbf{x}_a$  is the a priori state vector, and the regularization matrix  $\mathbf{R}$  is taken to be the inverse of the a priori covariance matrix  $\mathbf{S}_a$ .  $\mathbf{K}$  is the Jacobian matrix, and each column of  $\mathbf{K}$  contains the derivative of the spectrum with respect to an element of the state vector,  $\mathbf{K} = \frac{\partial f(\mathbf{x})}{\partial \mathbf{x}}$ . The Levenberg–Marquardt parameter  $\gamma$  is applied to a scaling matrix  $\mathbf{D}$ , which is also taken to be  $\mathbf{S}_a^{-1}$ . The Levenberg–Marquardt parameter affects the size of the state update so that smaller steps may be taken when the linearization of the forward model is not satisfactory.

The expected  $\chi^2$  of the maximum a posteriori probability solution should be

$$\chi^2(\hat{\mathbf{x}} - \mathbf{x}) = (\hat{\mathbf{x}} - \mathbf{x})^T \left( \mathbf{K}^T \mathbf{S}_y^{-1} \mathbf{K} + \mathbf{S}_a^{-1} \right) (\hat{\mathbf{x}} - \mathbf{x}) \approx n, \quad (\text{B3})$$

where  $n$  is the number of state vector elements. A solution is accepted when the ratio of the squared state update to the estimated variance is a negligible fraction of the expected  $\chi^2$ :

$$\Delta \mathbf{x} \left( \mathbf{K}^T \mathbf{S}_y^{-1} (\mathbf{y} - f(\mathbf{x}_i)) + \mathbf{S}_a^{-1} (\mathbf{x}_a - \mathbf{x}_i) \right) \ll n. \quad (\text{B4})$$

In an algorithm, “ $\ll n$ ” must use a specific limit, and in GFIT2, “ $< n/10$ ” was used. If the inequality check is made with a parameter that is too large, like “ $< n$ ”, the algorithm may take fewer iterations to converge but will take the same steps at each iteration, often leading to a retrieved profile closer to the a priori profile. The inequality check should be done with a small enough fraction of  $n$  that reducing it further does not significantly affect the solution.

If convergence is not reached in the  $i$ th iteration, an algorithm determines if the Levenberg–Marquardt parameter needs to be adjusted for the next iteration (Fletcher, 1971). Three different cost functions are used:

$$J_{\text{old}} = (\mathbf{y} - f(\mathbf{x}_i))^T \mathbf{S}_y^{-1} (\mathbf{y} - f(\mathbf{x}_i)) + (\mathbf{x}_a - \mathbf{x}_i)^T \mathbf{S}_a^{-1} (\mathbf{x}_a - \mathbf{x}_i), \quad (\text{B5})$$

$$J_{\text{new}} = (\mathbf{y} - f(\mathbf{x}_i + \Delta \mathbf{x}))^T \mathbf{S}_y^{-1} (\mathbf{y} - f(\mathbf{x}_i + \Delta \mathbf{x})) + (\mathbf{x}_a - \mathbf{x}_i - \Delta \mathbf{x})^T \mathbf{S}_a^{-1} (\mathbf{x}_a - \mathbf{x}_i - \Delta \mathbf{x}), \quad (\text{B6})$$

$$J_{\text{pred}} = (\mathbf{y} - f(\mathbf{x}_i) - \mathbf{K}\Delta\mathbf{x})^T \mathbf{S}_y^{-1} (\mathbf{y} - f(\mathbf{x}_i) - \mathbf{K}\Delta\mathbf{x}) + (\mathbf{x}_a - \mathbf{x}_i - \Delta\mathbf{x})^T \mathbf{S}_a^{-1} (\mathbf{x}_a - \mathbf{x}_i - \Delta\mathbf{x}), \quad (\text{B7})$$

where  $J_{\text{old}}$  is the cost function using the state vector at the beginning of the  $i$ th iteration,  $J_{\text{new}}$  is the cost function using the updated state vector at the end of the  $i$ th iteration, and  $J_{\text{pred}}$  is the cost function using the state vector update and the linear approximation:

$$f(\mathbf{x} + \Delta\mathbf{x}) \cong f(\mathbf{x}) + \mathbf{K}\Delta\mathbf{x}. \quad (\text{B8})$$

The ratio  $r$  is then evaluated:

$$r = \frac{J_{\text{new}} - J_{\text{old}}}{J_{\text{pred}} - J_{\text{old}}}. \quad (\text{B9})$$

This is the relative change in the cost function produced by a state vector update when using the forward model and a linear approximation of the forward model. The Levenberg–Marquardt parameter is then adjusted as follows:

- $r > 0.75$ . The linearization of the forward model is satisfactory and  $\gamma$  is reduced to allow larger steps.
  - $\gamma = \frac{\gamma}{2}$
- $r \geq 0.25$ . Intermediate case, make no change to  $\gamma$  and reset the number of consecutive divergences.
  - $\text{ndiv} = 0$
- $r < 0.25$ . The linearization of the forward model is not satisfactory, increment the number of consecutive divergences,  $\gamma$  is increased to take smaller steps.
  - $\text{ndiv} = \text{ndiv} + 1$
  - if  $\gamma = 0$  then  $\gamma = 1$
  - if  $\gamma > 0$  then  $\gamma = 10\gamma$

If  $\text{ndiv}$  reaches some specified maximum number, there will not be another iteration. When  $r < 0.25$ , it means that the linearization of the forward model is not good enough. In GFIT2, this was not allowed to happen more than twice in a row. Increasing  $\gamma$  will lead to a smaller step for the state vector update, increasing the chance that the linearization of the forward model at the next step will be better and  $r \geq 0.25$ .

In GFIT2  $r > 0.75$  in most cases, and if  $\gamma$  is not initially set to 0 it will tend towards zero until the convergence criterion is met; thus the initial value of  $\gamma$  was set to 0. However, the increase of the parameter is often triggered when fitting noisier spectra and can give the algorithm a chance to converge when it would otherwise need more iterations or fail without  $\gamma$ .

After the last iteration, the goodness of the retrieval is checked by evaluating the reduced  $\chi^2$  of the spectral residuals.

$$\chi_{\text{red}}^2(\mathbf{y} - f(\mathbf{x})) = \frac{1}{N} \sum_{i=1}^N \left( \frac{y_i - f(\mathbf{x})_i}{y_{\text{noise}}} \right)^2, \quad (\text{B10})$$

where  $y_{\text{noise}}$  is the measurement uncertainty, and  $N$  is the number of spectral points. Profile retrievals from real spectra are presented in Sect. 3 where the root mean square of the residuals from a scaling retrieval is used as  $y_{\text{noise}}$ . In that case Eq. (B10) is the average ratio of residuals (RR) between the profile and scaling retrieval.

The retrieval covariance matrix is

$$\hat{\mathbf{S}} = \left( \mathbf{K}^T \mathbf{S}_y^{-1} \mathbf{K} + \mathbf{S}_a^{-1} \right)^{-1}. \quad (\text{B11})$$

The square root of its diagonal elements is used as the uncertainty in the retrieved scaling factors.

### Appendix C: Averaging kernel

The state vectors of GFIT and GFIT2 contain scaling factors to be applied to a priori mole fractions. The averaging kernel matrix is

$$\mathbf{A} = \left( \mathbf{K}^T \mathbf{S}_y^{-1} \mathbf{K} + \mathbf{S}_a^{-1} \right)^{-1} \mathbf{K}^T \mathbf{S}_y^{-1} \mathbf{K}. \quad (\text{C1})$$

It is a change in the retrieved state for a change in the state vector elements.

$$(\mathbf{A}_{\text{SF}})_{i,j} = \frac{\delta \hat{x}_i}{\delta x_j} \quad (\text{C2})$$

Even though the averaging kernel is dimensionless, its units can be written as, for example, “ppm per ppm” to indicate that it is the change at a given level for a change at a different level.

To obtain the averaging kernel in ppm per ppm,

$$(\mathbf{A}_{\text{vmr}})_{i,j} = (\mathbf{A}_{\text{SF}})_{i,j} \frac{\text{vmr}_i}{\text{vmr}_j}, \quad (\text{C3})$$

where  $\text{vmr}$  is the a priori mole fraction at the  $i$ th and  $j$ th levels and the partial column averaging kernel matrix in molecules  $\text{cm}^{-2}$  per molecules  $\text{cm}^{-2}$  is

$$(\mathbf{A}_{\text{col}})_{i,j} = (\mathbf{A}_{\text{SF}})_{i,j} \frac{\text{vmr}_i \times d_i \times \text{sp}_i}{\text{vmr}_j \times d_j \times \text{sp}_j}, \quad (\text{C4})$$

where  $\text{sp}$  denotes the widths of the slant layers along the sun ray that correspond to the altitude levels of the prescribed vertical grid. The total column averaging kernel vector can be obtained from the partial column averaging kernel matrix:

$$\mathbf{a}_j = \sum_{i=1}^{\text{nlev}} (\mathbf{A}_{\text{col}})_{i,j}. \quad (\text{C5})$$

It represents the change in the total column (molecules  $\text{cm}^{-2}$ ) caused by a change in the partial column of the  $j$ th layer. It should ideally be equal to 1 at each level, meaning that adding  $N$  target molecules anywhere in the atmosphere will lead to  $N$  more molecules in the retrieved total column.

The averaging kernel matrix would ideally be an identity matrix, meaning that adding  $N$  molecules in the  $j$ th layer would lead to  $N$  more molecules retrieved in that layer. However, adding  $N$  molecules in the  $j$ th layer will lead to an increase in the width of CO<sub>2</sub> absorption lines of a spectrum observed from the ground. As illustrated for CO<sub>2</sub> in Fig. 2, each wavenumber is affected by the CO<sub>2</sub> concentration over a range of altitudes, because the spectrum observed on the ground is the product of all the spectra that would be observed at each altitude. Even if that change in line widths was the only change in the spectrum and could be fitted perfectly, it would be impossible to exactly attribute that change to a specific level. Although the total column averaging kernel could be exactly 1 at each level, the averaging kernel matrix can never be exactly the identity matrix for direct-sun measurements from the ground.

The column averaging kernel matrix can be used to degrade higher-resolution profiles before comparing them to retrieved profiles (Rodgers and Connor, 2003).

$$\mathbf{c}_s = \mathbf{A}_{\text{col}} (\mathbf{c} - \mathbf{c}_a) + \mathbf{c}_a, \quad (\text{C6})$$

where  $\mathbf{c}_s$  is the smoothed partial column profile,  $\mathbf{c}$  is the partial column profile to be smoothed, and  $\mathbf{c}_a$  is the a priori partial column profile. Or, using the total column averaging kernel,

$$\mathbf{c}_s^{\text{tot}} = \mathbf{c}_a^{\text{tot}} + \mathbf{a}^T (\mathbf{c} - \mathbf{c}_a), \quad (\text{C7})$$

where  $\mathbf{a}^T$  is the transpose of  $\mathbf{a}$ , and the “tot” superscript indicates a total column:

$$\mathbf{c}_a^{\text{tot}} = \sum_{i=1}^{\text{nlev}} \mathbf{c}_{a_i}. \quad (\text{C8})$$

#### Appendix D: Information content and error analysis

The singular value decomposition of the CO<sub>2</sub> Jacobian matrix can provide information on the relative precision with which different vertical patterns are measured. The Jacobian matrix  $\mathbf{K}$  is decomposed into

$$\mathbf{K}(\text{nmp}, \text{nlev}) = \mathbf{U}(\text{nmp}, \text{nlev}) \mathbf{L}(\text{nlev}, \text{nlev}) \times \mathbf{V}^T(\text{nlev}, \text{nlev}), \quad (\text{D1})$$

where nmp is the number of measured spectral points, nlev is the number of atmospheric levels,  $\mathbf{U}$  is the matrix of left singular vectors,  $\mathbf{L}$  is the diagonal matrix of singular values, and  $\mathbf{V}^T$  is the transpose of the matrix of right singular vectors. The right singular vectors of  $\mathbf{K}$  associated with the eight largest singular values are shown in Figs. D1 to D5 for each CO<sub>2</sub> band on 14 January 2012. The right singular vectors represent independently measured vertical patterns with a precision indicated by their corresponding singular values shown above each panel. The singular values are also shown as a

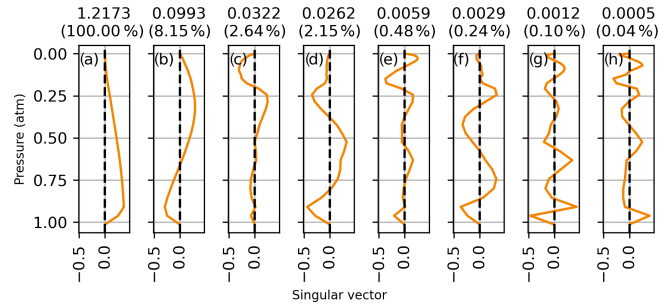


**Figure D1.** Right singular vector of the Jacobian associated with the eight largest singular values for profile retrievals from the Strong CO<sub>2</sub> window on 14 January 2012. The singular values are shown above each panel, and the singular value normalized to the largest singular value is shown in parenthesis.

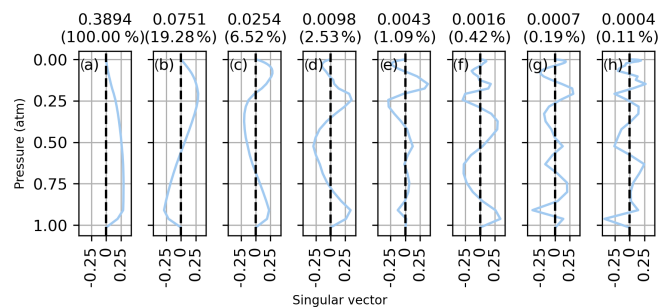


**Figure D2.** Same as Fig. D2 but for the TCCON1 window.

fraction of the largest singular value in parenthesis. The singular vectors all show an increasing number of oscillations with decreasing singular value. In each window, the first singular vector is close to a uniform weighting at all altitudes and has 3 to 10 times more sensitivity than the second pattern. The singular vector in panel (d) has a structure like that of the CO<sub>2</sub> profile deviations observed in the sensitivity tests of Sect. 3.1.

The retrieval covariance matrix  $\hat{\mathbf{S}}$  can be expressed as a sum of the null space covariance  $\mathbf{S}_N$  and the measurement noise covariance  $\mathbf{S}_m$  (Rodgers, 1990):

$$\mathbf{S}_N = \left( \mathbf{S}_a^{-1} + \mathbf{K}^T \mathbf{S}_y^{-1} \mathbf{K} \right)^{-1} \mathbf{S}_a^{-1} \left( \mathbf{S}_a^{-1} + \mathbf{K}^T \mathbf{S}_y^{-1} \mathbf{K} \right)^{-1}, \quad (\text{D2})$$

$$\mathbf{S}_m = \left( \mathbf{S}_a^{-1} + \mathbf{K}^T \mathbf{S}_y^{-1} \mathbf{K} \right)^{-1} \mathbf{K}^T \mathbf{S}_y^{-1} \times \mathbf{K} \left( \mathbf{S}_a^{-1} + \mathbf{K}^T \mathbf{S}_y^{-1} \mathbf{K} \right)^{-1}. \quad (\text{D3})$$

The error patterns of these matrices hold information on vertical structures in the CO<sub>2</sub> profiles that the retrieval cannot resolve, due to the smoothing effect of the a priori covariance matrix  $\mathbf{S}_a$  in the case of  $\mathbf{S}_N$ , and due to the effect of measurement noise in the case of  $\mathbf{S}_m$ , as the measurement error covariance matrix  $\mathbf{S}_y$  only represents random errors in the measured radiances. The error patterns of a matrix are defined as its eigenvectors multiplied by the square root of their cor-

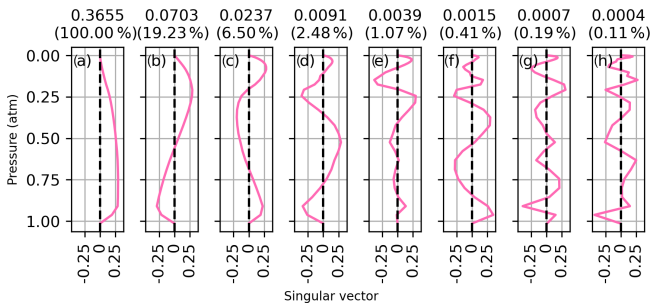


**Figure D3.** Same as Fig. D1 but for the TCCON2 window.

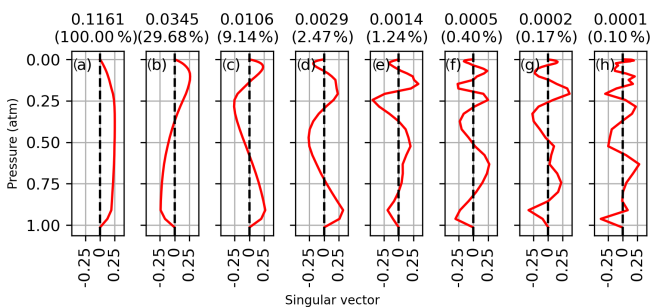


**Figure D4.** Same as Fig. D1 but for the Weak1 window.

responding eigenvalue. The error patterns of  $\mathbf{S}_N$  associated with the four largest eigenvalues are shown in Fig. D6, and those of  $\mathbf{S}_m$  are shown in Fig. D7. In both cases, the largest error pattern peaks at the surface and falls to 0 at  $\sim 0.9$  atm; these peaks in the error patterns correspond to a minimum in the singular vectors of the CO<sub>2</sub> Jacobian. The large errors in the retrieved CO<sub>2</sub> profiles are explained by the larger a priori uncertainty in the lower troposphere, and by the relatively larger effect of errors at wavenumbers strongly weighted at low altitudes. This is because “sensitivity” is determined by the Jacobian; the retrieval will simply preferentially adjust CO<sub>2</sub> at levels where a given change in CO<sub>2</sub> causes a larger change in radiance. At pressures larger than  $\sim 0.9$  atm, the error patterns of  $\mathbf{S}_N$  represent vertical scales that cannot be resolved in the retrieval, with a vertical scale of 0.3 atm or less.

The uncertainty in the retrieved CO<sub>2</sub> profile is taken to be the square root of the diagonal elements of  $\hat{\mathbf{S}}$  even though the retrieval covariance is not diagonal. It is presented in Fig. D8 as a percentage of the a priori uncertainties. The retrieval error is always smaller than the a priori covariance by construction in optimal estimation, so this alone gives no indication of a successful retrieval. But the retrieval is more sensitive to altitudes where the retrieval uncertainty is a smaller fraction of the a priori uncertainty. The error from the diagonal of  $\mathbf{S}_N$  and  $\mathbf{S}_m$  is also shown. In addition to  $\mathbf{S}_N$ , the smoothing contribution from state vector elements other than CO<sub>2</sub> scale factors is shown as  $\mathbf{S}_i$ , the interference error covariance

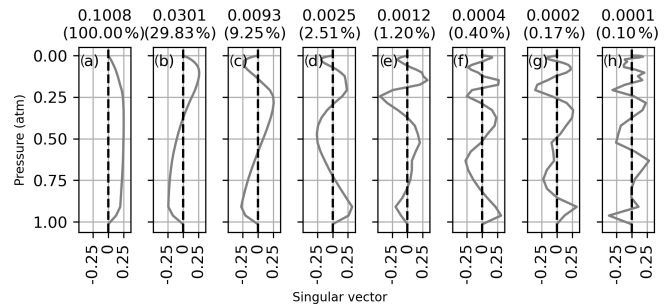


**Figure D5.** Same as Fig. D1 but for the Weak2 window.

(Rodgers and Connor, 2003):

$$\mathbf{S}_i = \mathbf{A}_{xe} \mathbf{S}_{a,e} \mathbf{A}_{xe}^T \quad (\text{D4})$$

where  $\mathbf{S}_{a,e}$  is the part of the a priori covariance matrix that corresponds to “extra” state vector elements other than CO<sub>2</sub> scale factors. With  $N$  total state vector elements and  $n_{lev}$  atmospheric levels,  $\mathbf{S}_{a,e}$  has dimensions  $(N-n_{lev}, N-n_{lev})$ .  $\mathbf{A}_{xe}$  is the subset of the averaging kernel matrix that characterizes the smoothing effect of the extra state vector elements on the CO<sub>2</sub> profiles, with dimensions  $(n_{lev}, N-n_{lev})$ . The interference error is the smallest contribution to the total error and most of the error comes from the smoothing effect of the a priori CO<sub>2</sub> covariance, followed by the contribution of measurement noise which oscillates between  $\sim 10\%$ – $25\%$  of the a priori CO<sub>2</sub> uncertainty. If temperature were retrieved, for example with a temperature offset or with a scale factor added to the extra state vector elements, we would expect the interference error to increase.

## Appendix E: Empirical corrections

In Sect. 3 we saw that CO<sub>2</sub> profile retrievals have high sensitivity to CO<sub>2</sub> in the absence of errors in the a priori meteorology and systematic errors in instrument line shape. Here we investigate the possibility of empirically removing the effect of those errors by de-weighting systematic spectral fitting residuals using empirical orthogonal functions (EOFs). EOFs have been used, for example, with retrievals from GOSAT and OCO-2 measurements (O’Dell et al., 2018).

### E1 Empirical orthogonal functions

To reduce the effect of systematic residuals on retrieved profiles, EOFs of the spectral fitting residuals were derived to find and remove systematic patterns in the residuals related to temperature errors, instrument line shape, and other effects. The residuals divided by air mass from a set of retrievals covering a wide range of observational conditions are stored in a matrix  $\mathbf{M}(m, n)$ , with  $n$  the number of spectra and  $m$  the number of spectral points. Then a singular value decomposition is performed on this matrix. The columns of the matrix of left singular vectors are orthogonal basis vectors of

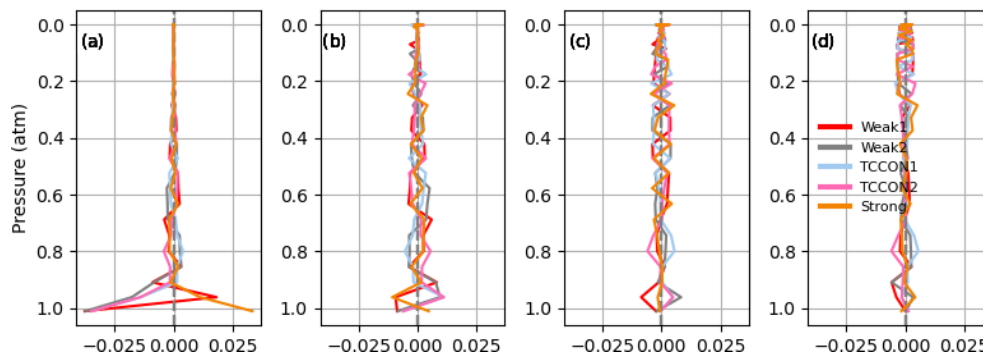


**Figure D6.** The four largest error patterns of the null space covariance matrix for a Lamont spectrum measured on 14 January 2012.

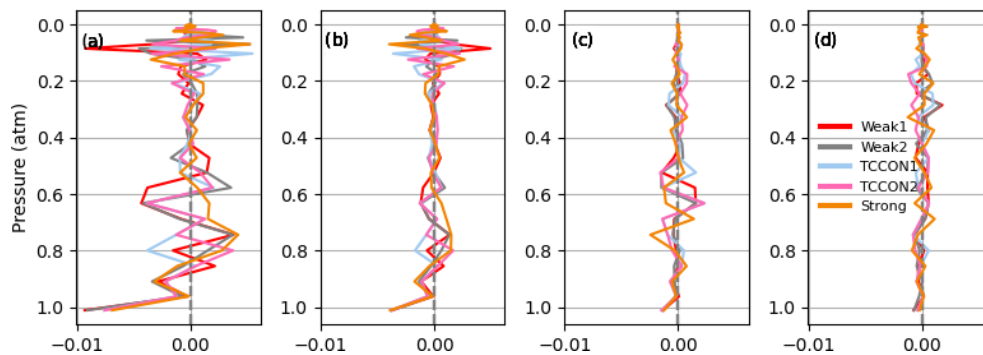


**Figure D7.** Same as Fig. D6 but for the measurement noise covariance matrix.

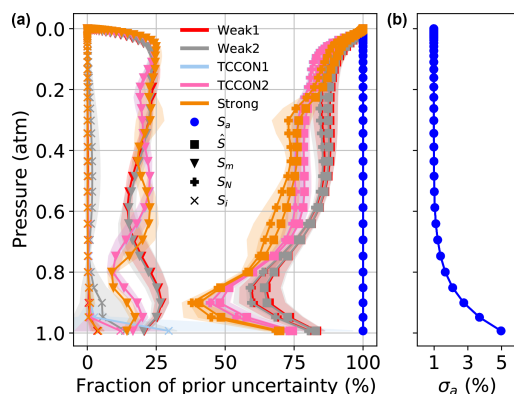


**Figure D8.** Panel (a) shows the square root of the diagonal elements of the retrieval total error covariance matrix  $\hat{S}$ , the null space covariance matrix  $S_N$ , the interference error covariance matrix  $S_I$ , and the measurement noise error covariance matrix  $S_m$  expressed as a fraction of the a priori uncertainty  $\sigma_a$ . Each line is the average from the set of 8 days with AirCore measurements over Lamont, and the bands indicate the standard deviation. Panel (b) shows the a priori uncertainty.

the residuals and those associated with the largest singular values represent the main patterns in the residuals, while the corresponding right singular vectors can provide information on the temporal frequency of these patterns.

We use a linear combination of left singular vectors. Each singular vector is associated with a scaling factor. The scaling factor is part of the state vector and adjusted during the retrieval using 100 % uncertainty. Before each inversion step, the spectrum “ $c$ ” calculated with the forward model becomes:

$$c = c + \sum_{i=1}^N a_i u_i, \quad (\text{E1})$$

where  $N$  is the number of EOFs to use, ordered with decreasing singular value. The first EOF, associated with the highest singular value, is like the scaled average residual from all the spectral residuals in the matrix  $M$ . Our implementation differs from that described by O’Dell et al. (2018) in that here the EOFs are derived from a set of residuals obtained using scaling retrievals, and not using profile retrievals. Since they are meant to remove systematic errors in the calculated spectra before the retrieval adjusts the CO<sub>2</sub> scaling factors, the EOFs should be derived from a large set of residuals obtained with scaling retrievals to have a significant effect on the profile retrieval. If they are derived from residuals obtained with profile retrievals, these mainly include systematic error patterns corresponding to interfering species, which are not the main source of deviations in retrieved CO<sub>2</sub> profiles. When using scaling retrieval residuals, each EOF includes different error patterns corresponding to CO<sub>2</sub> absorption lines. These

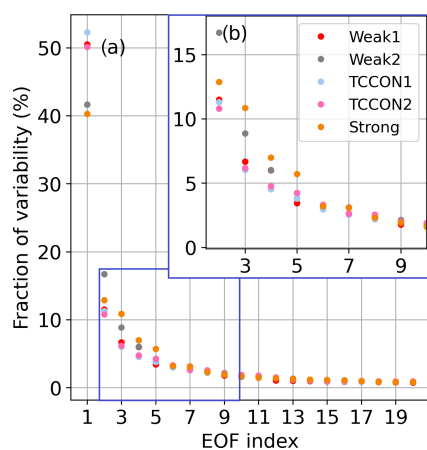


**Figure E1.** Fraction of the variability in the spectral residuals accounted for by each empirical orthogonal function in each CO<sub>2</sub> window. The EOF numbers are shown in decreasing order of singular value. Panel (b) highlights the blue rectangle inside panel (a).

error patterns may be attributed to systematic errors for the first EOF, such as errors in spectroscopy, or in the instrument line shape, or a persistent bias in meteorology. The error patterns can also correspond to errors in the a priori meteorology. The temporal frequency of each error pattern is contained in the corresponding right singular vector. The right singular vectors could help diagnose, for example, biases in a priori temperature profiles on different timescales. The right singular vectors can also be used to find correlations between each spectral residual pattern and other quantities measured in time, such as differences between a priori and measured meteorology.

If the residual patterns corresponding to CO<sub>2</sub> lines have the same shape as residuals caused by errors in the a priori CO<sub>2</sub> profile shape, adjustments to the CO<sub>2</sub> scaling factors will compete with adjustments to the EOF scaling factors in the retrieval. Because higher-order EOFs are associated with residuals with different time periodicity, they can also introduce errors that do not exist in calculated spectra. We chose to only include the first EOF, which represents residual patterns common to most spectra. The leading EOF can explain 40 % to 52 % of the variability in the residuals, depending on the window, as shown in Fig. E1. The fraction of variability is obtained as the singular value of a given EOF divided by the sum of all singular values. The first 10 EOFs in each window are above the noise level of singular values and account for over 90 % of the variability in the residuals.

## E2 Results

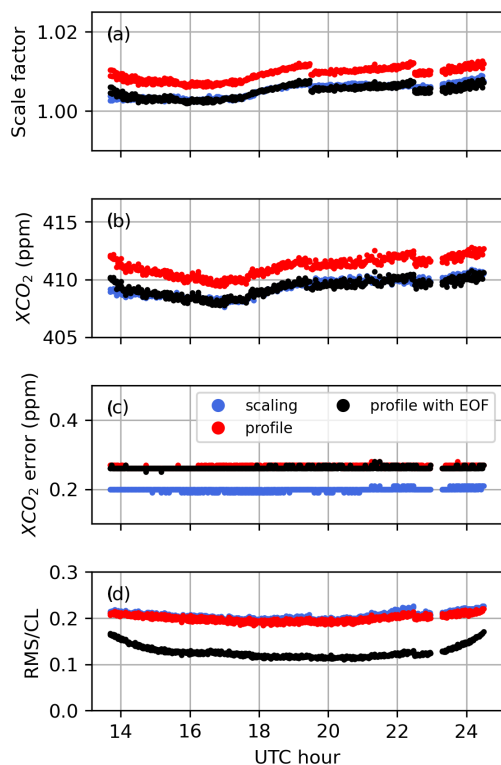
One year of measurements from the East Trout Lake (SK, Canada) TCCON station were processed in three ways: with scaling retrievals, with profile retrievals, and with profile retrievals including the first EOF derived from residuals obtained with the scaling retrievals. The residuals used to derive the EOFs are filtered such that spectra that would not pass the TCCON quality checks are not included. To avoid isolated spectra with large residuals having a disproportionate impact on the singular value decomposition of the matrix of residuals, all the spectra are ordered by increasing solar zenith angle and filtered based on the root mean square of the residuals: the 500-point rolling median is computed, and the median of the 500-point rolling standard deviation is used as an estimate of the standard deviation  $\sigma$ ; then only spectra within  $1\sigma$  of the rolling median for all windows are used to derive the EOFs. The matrix of residuals resulting from this filtering includes 42 037 out of 64 245 total spectra. XCO<sub>2</sub> was retrieved from each window separately. The statistics on the retrieved XCO<sub>2</sub> error are shown in Table E1 for each retrieval type and for each window. In all windows but the Strong window, the changes in XCO<sub>2</sub> error between the different retrieval methods are small, less than 0.05 ppm. This is 8 times smaller than the reported TCCON  $1\sigma$  single-measurement precision of 0.4 ppm. However, the mean XCO<sub>2</sub> error is  $\sim 55\%$  larger in the strong window with profile retrievals compared to scaling retrievals.

Figures E2 to E6 show quantities derived from each type of retrieval for an example day and for each window. In each window, the profile retrieval with the first EOF appears as an intermediate case between the profile retrieval and the scaling retrieval. In each case, the root mean square of the residuals is smaller for profile retrieval with the first EOF, but the XCO<sub>2</sub> error is not necessarily smaller.

In Fig. E7a, XCO<sub>2</sub> differences are shown between profile and scaling retrievals, and between profile retrievals including the first EOF and scaling retrievals in Fig. E7b. We have seen that differences in XCO<sub>2</sub> error between the different retrieval types are within 0.05 ppm. However, differences in XCO<sub>2</sub> between profile and scaling retrievals can be several times larger than the XCO<sub>2</sub> error, indicating different sources of bias between profile and scaling retrievals. In the Weak1 window, the median of the XCO<sub>2</sub> absolute differences are  $\sim 4$  times larger than the median XCO<sub>2</sub> error and  $\sim 3$  times larger in the Strong window. In the TCCON1, TCCON2, and Weak2 windows, the median of the XCO<sub>2</sub> absolute difference is smaller than the median XCO<sub>2</sub> error. In all but the Weak1 window, the XCO<sub>2</sub> differences are 25 % to 35 % smaller between August and November than for the rest of the year. In Fig. E7b, the XCO<sub>2</sub> differences between the profile retrievals with EOF and the scaling retrievals are smaller and more consistent between windows than in Fig. E7a. And the median of the XCO<sub>2</sub> absolute differences is smaller than the median XCO<sub>2</sub> error in all windows. Including the leading

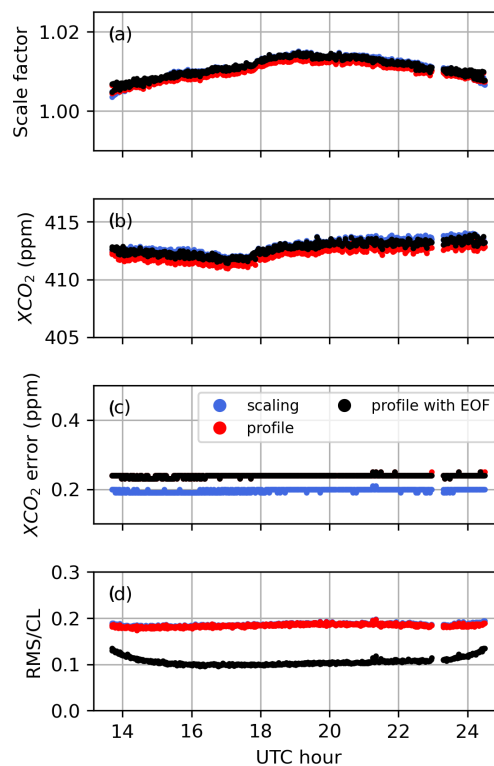
**Table E1.** Statistics on the retrieved XCO<sub>2</sub> error for one year of measurements at the East Trout Lake TCCON station. “SD” indicates the standard deviation.

XCO <sub>2</sub> error (ppm)	Scaling retrieval			Profile retrieval			Profile retrieval with the first EOF		
Window	Mean	Median	SD	Mean	Median	SD	Mean	Median	SD
Strong	0.51	0.38	0.37	0.79	0.63	0.60	0.78	0.61	0.59
Weak1	0.89	0.64	0.68	0.91	0.67	0.66	0.90	0.66	0.66
Weak2	0.80	0.56	0.64	0.81	0.61	0.56	0.80	0.61	0.56
TCCON1	0.74	0.48	0.66	0.79	0.51	0.70	0.79	0.51	0.70
TCCON2	0.69	0.45	0.61	0.74	0.47	0.66	0.74	0.47	0.66

**Figure E2.** Quantities derived from retrievals on East Trout Lake measurements on 29 March 2018 for the Strong window. The retrieval type is indicated by the legend. Panel (a) shows the column-integrated CO<sub>2</sub> scale factor. Panel (b) shows XCO<sub>2</sub> and panel (c) shows the XCO<sub>2</sub> error. Panel (d) shows the root mean square of the residuals as a fraction of the continuum level.

EOF in a profile retrieval reduces the XCO<sub>2</sub> differences between the scaling and profile retrievals, but the XCO<sub>2</sub> of the profile retrieval with EOF is more strongly correlated with the XCO<sub>2</sub> of the profile retrieval than that of the scaling retrieval as shown in Table E2.

When compared to preliminary data from aircraft measurements, the deviations in the CO<sub>2</sub> profiles obtained with profile retrievals are larger than the vertical variations in the aircraft measurement. When the retrieved profiles present

**Figure E3.** Same as Fig. E2 but for the TCCON1 window.**Table E2.** Squared Pearson correlation coefficient for XCO<sub>2</sub> between the scaling and profile retrievals (SCL–PRF), and between the profile retrieval with the first EOF and the profile retrieval (EOF–PRF).

$R^2$	SCL–PRF	EOF–PRF
Strong	0.9368	0.9929
Weak1	0.9633	0.9951
Weak2	0.9586	0.9814
TCCON1	0.9922	0.9995
TCCON2	0.9931	0.9999

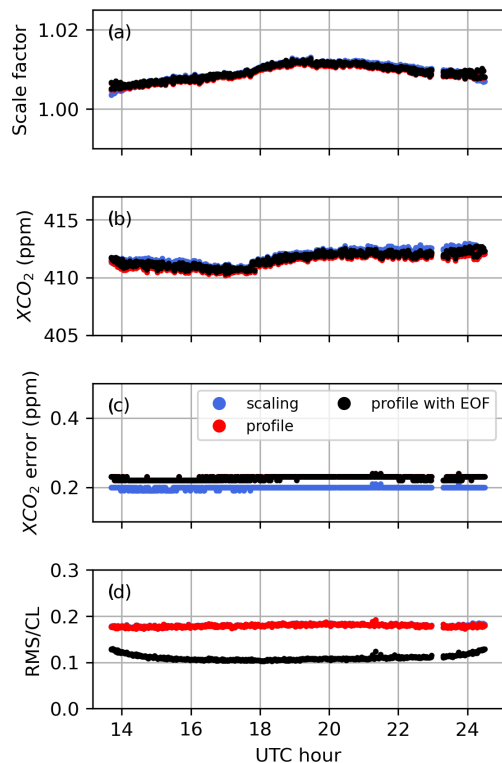


**Figure E4.** Same as Fig. E2 but for the TCCON2 window.

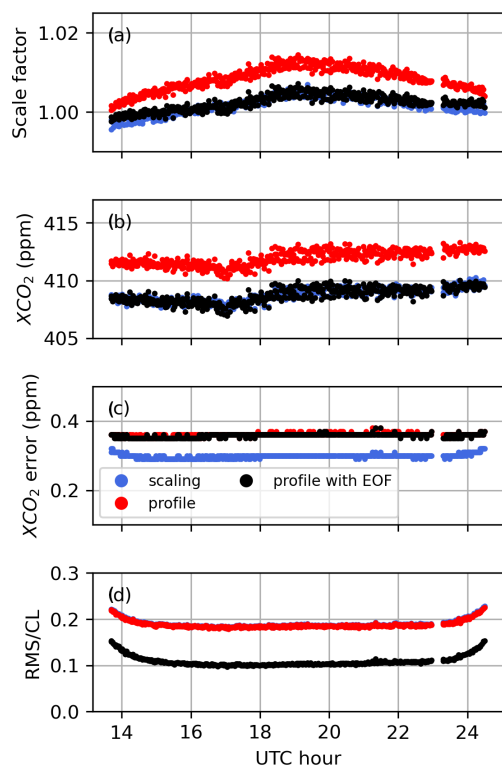


**Figure E5.** Same as Fig. E2 but for the Weak1 window.

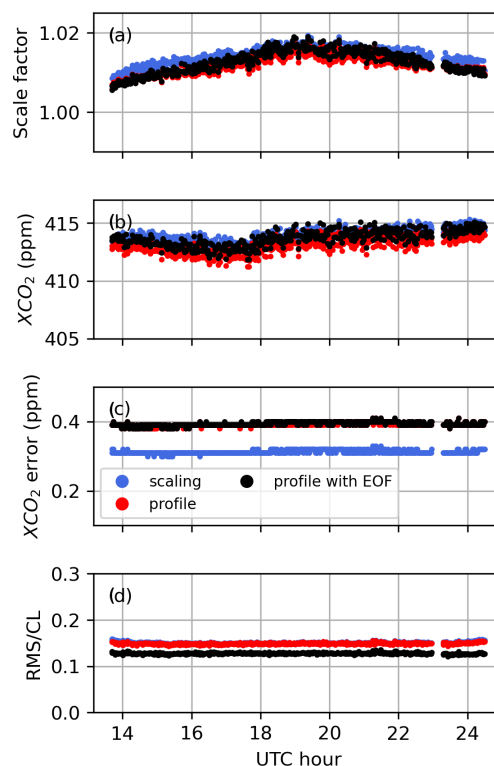


**Figure E6.** Same as Fig. E2 but for the Weak2 window.

large deviations typical of temperature errors like that in Fig. 9b, the CO<sub>2</sub> profile obtained from profile retrieval with the first EOF reduces the amplitude of the deviations, but the shape persists. This is expected as the first EOF represents the average residuals, which should not include residual features caused by temperature errors, unless the temperature errors were always biased in the same way. We would expect the first EOF to reduce deviations like that in Fig. 9a. In such cases, the CO<sub>2</sub> profiles obtained from profile retrieval with the first EOF are smoother than profile retrievals but present no clear advantage over scaling retrievals.

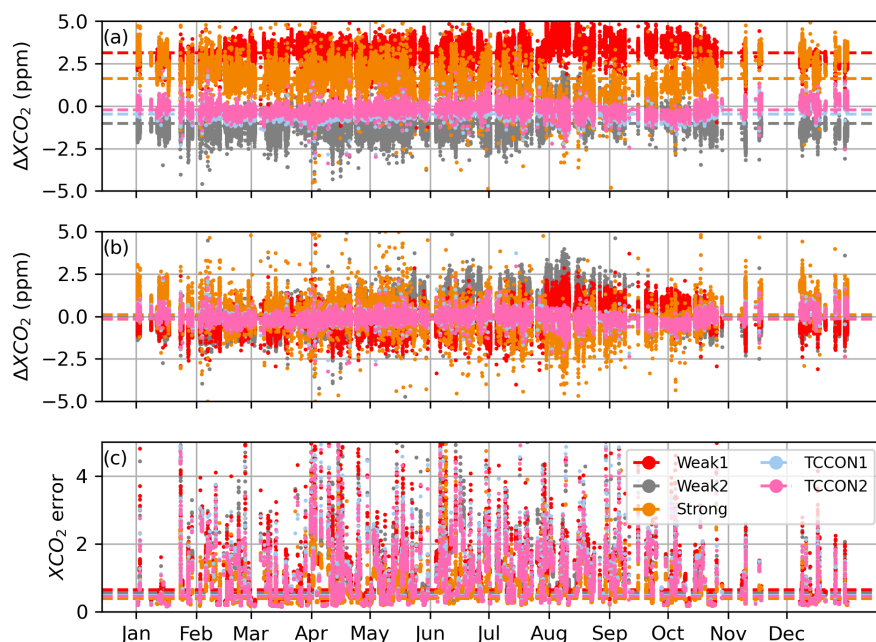


**Figure E7.** In panel (a), the XCO<sub>2</sub> obtained from the scaling retrieval is subtracted from the XCO<sub>2</sub> obtained from the profile retrieval. In panel (b), the XCO<sub>2</sub> obtained from the scaling retrieval is subtracted from the XCO<sub>2</sub> obtained from the profile retrieval with EOF. In panel (c), the XCO<sub>2</sub> error from the scaling retrieval is shown, with the median values as dashed lines. In the top two panels, the horizontal dashed lines show the median values of absolute differences in XCO<sub>2</sub>.

#### Appendix F: Synthetic spectra, perturbed field of view and zero-level offset

The saturated lines of the Strong window allow a zero-level offset to be fit. Figure F1 shows the zero-level offset retrieved from the Strong window using real spectra for each of the days with Lamont data used in Sect. 3. The median absolute value is at most 0.001 on 23 July 2013. The effect of a zero-level offset on retrieved profiles was tested with synthetic spectra. Figure F2a and b are the same as Fig. 4a and b and show profiles retrieved from synthetic spectra in the reference case, when no perturbation is applied. Figure F2e and f show the effect of a +0.002 perturbation to the zero-level offset, without retrieving it in the Strong window. This has a large effect in the profile retrieved from the Strong window, with deviations from the truth within 30 ppm, and a smaller effect in the other bands with deviations up to 10 ppm.

In Fig. F2c and d we also consider the effect of one type of ILS error by perturbing the internal field of view by +7 %, which leads to a widening of the ILS. The unperturbed internal field of view of the spectrometer is 2.4 mrad. The deviations from the truth are within 1 ppm for  $P > 0.5$  atm and within 3 ppm for  $P < 0.5$  atm.

This sensitivity test shows the effect of zero-level offsets will not be a major source of variability in the retrieved profiles. If the zero-level offset retrieved from the Strong window is added to the TCCON and Weak windows before the retrieval, the change in the retrieved profiles is less than

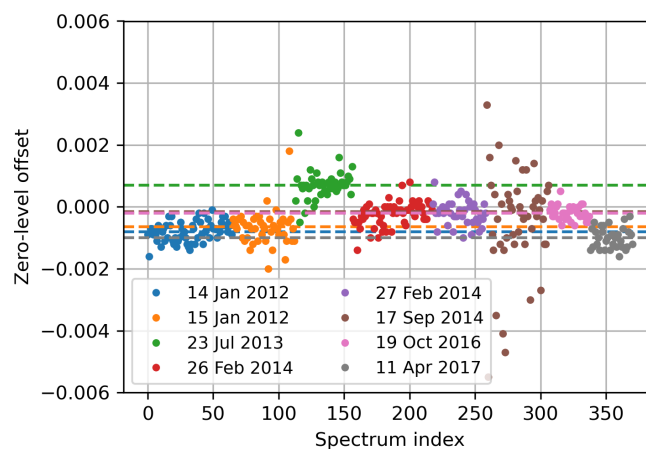


**Figure F1.** Zero-level offset retrieved from the Strong CO<sub>2</sub> window for the Lamont spectra coincident within  $\pm 1$  h of the last AirCore sampling time and within  $\pm 1.5$  h of the closest a priori time on each of the days indicated by the legend. The dashed lines mark the median value for each date.

3 ppm at all altitudes as shown in Fig. F3 using days with AirCore profiles at Lamont.

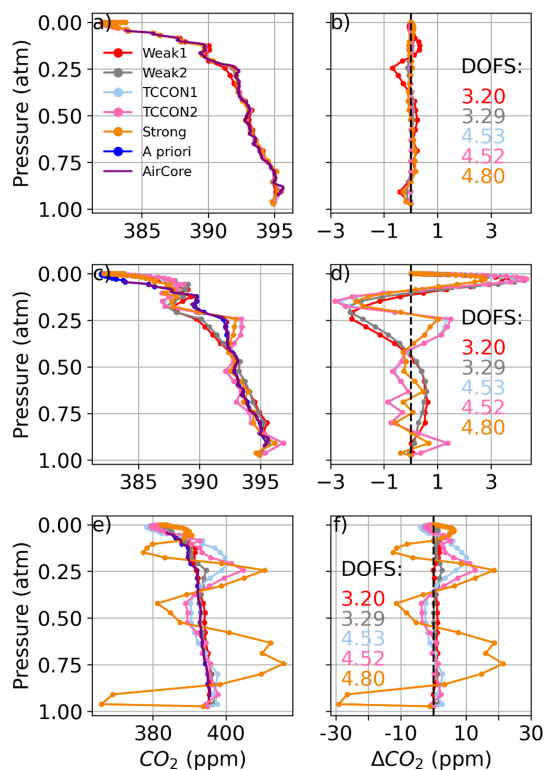


**Figure F2.** The left-hand panels show CO<sub>2</sub> profiles retrieved using synthetic spectra. In (a), we use the AirCore profile, which was used to generate the synthetic spectra, as the a priori profile. In (c), the internal field of view is perturbed by +7 %, increasing the width of the ILS. In (e), the zero-level offset is perturbed by +0.002 and is not retrieved in the Strong window. Panels (b), (d), and (f) show the difference between the retrieved profiles and AirCore, corresponding to (a), (c), and (e) respectively.

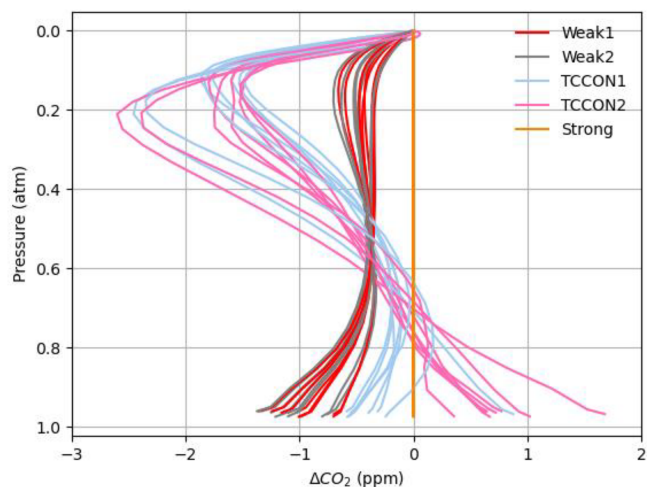


**Figure F3.** Using real Lamont spectra with the AirCore profile as the a priori profile, the zero-level offset was first retrieved from the Strong window and then added in the Weak and TCCON windows. The difference in the retrieved profiles with and without the added offset is shown for each window and for all the days with AirCore profiles over Lamont. In the Strong window, where the offset is retrieved, the differences are less than 0.001 ppm.

*Code availability.* It is our intention to make the profile retrieval code available as part of a future version of GGG and hence publicly available through TCCON; until then it can be made available upon request to the corresponding author.

*Data availability.* The data used in this study consist of synthetic spectra generated with GGG2020 and measured spectra from the Lamont and East Trout Lake TCCON stations. Scaling retrieval products from those sites using the GGG2014 algorithm (<https://doi.org/10.14291/tcon.ggg2014.lamont01.r1/1255070>, Wennberg et al., 2016; <https://doi.org/10.14291/tcon.ggg2014.eastroutlake01.r1>, Wunch et al., 2018) are available publicly through CaltechDATA (<https://tcondata.org>, last access: 13 November 2020). Measured solar absorption spectra can be obtained by contacting the TCCON site PIs.

*Author contributions.* SR analyzed the data and prepared the paper with detailed feedback from all co-authors. JM implemented qSDV+LM into GFIT and provided guidance for its use with GFIT2. BJC wrote the initial GFIT2 algorithm and SR implemented changes relevant to this study. GCT is the author of GGG and provided support and significant conceptual input with DW, KS, and BJC. JLL and SR developed the code to generate the GGG2020 a priori profiles. The East Trout Lake solar spectra were provided by DW and JM. CS and BB provided the AirCore data. SCB provided the Lamont surface and aircraft measurements.

*Competing interests.* The authors declare that they have no conflict of interest.

*Acknowledgements.* The GEOS-5-FPIT data used in this study have been provided by the Global Modeling Assimilation Office (GMAO) at NASA Goddard Space Flight Center. The Lamont solar spectra were provided by Coleen Roehl and Paul Wennberg from the California Institute of Technology. The Lamont TCCON site operates with funding from NASA. In situ observations and vertical profiles collected over the Southern Great Plains were supported by the Office of Biological and Environmental Research of the US Department of Energy under contract no. DE-AC02-05CH11231 as part of the Atmospheric Radiation Measurement (ARM) Program, ARM Aerial Facility (AAF), and Terrestrial Ecosystem Science (TES) Program. The GNU parallel package (Tange, 2011) has been used to run tests with GFIT2.

*Financial support.* This research has been supported by the Natural Sciences and Engineering Research Council of Canada (grant no. 433842-2012) and the Canadian Space Agency (grant no. 45-7014551).

*Review statement.* This paper was edited by Frank Hase and reviewed by two anonymous referees.

## References

- Andrews, A. E., Boering, K. A., Daube, B. C., Wofsy, S. C., Loewenstein, M., Jost, H., Podolske, J. R., Webster, C. R., Herman, R. L., Scott, D. C., Flesch, G. J., Moyer, E. J., Elkins, J. W., Dutton, G. S., Hurst, D. F., Moore, F. L., Ray, E. A., Romashkin, P. A., and Strahan, S. E.: Mean ages of stratospheric air derived from in situ observations of CO<sub>2</sub>, CH<sub>4</sub>, and N<sub>2</sub>O, *J. Geophys. Res.-Atmos.*, 106, 32295–32314, <https://doi.org/10.1029/2001JD000465>, 2001.
- Aumann, H. H., Chahine, M. T., Gautier, C., Goldberg, M. D., Kalnay, E., McMillin, L. M., Revercomb, H., Rosenkranz, P. W., Smith, W. L., Staelin, D. H., Strow, L. L., and Susskind, J.: AIRS/AMSU/HSB on the aqua mission: Design, science objectives, data products, and processing systems, *IEEE Trans. Geosci. Remote Sens.*, 41, 253–263, <https://doi.org/10.1109/TGRS.2002.808356>, 2003.
- Basu, S., Baker, D. F., Chevallier, F., Patra, P. K., Liu, J., and Miller, J. B.: The impact of transport model differences on CO<sub>2</sub> surface flux estimates from OCO-2 retrievals of column average CO<sub>2</sub>, *Atmos. Chem. Phys.*, 18, 7189–7215, <https://doi.org/10.5194/acp-18-7189-2018>, 2018.
- Benner, D. C., Devi, V. M., Sung, K., Brown, L. R., Miller, C. E., Payne, V. H., Drouin, B. J., Yu, S., Crawford, T. J., Mantz, A. W., Smith, M. A. H., and Gamache, R. R.: Line parameters including temperature dependences of air- and self-broadened line shapes of <sup>12</sup>C<sup>16</sup>O<sub>2</sub>: 2.06- $\mu$ m region, *J. Mol. Spectrosc.*, 326, 21–47, <https://doi.org/10.1016/j.jms.2016.02.012>, 2016.
- Biraud, S. and Moyes, A.: Atmospheric Radiation Measurement (ARM) user facility. Updated hourly. Precision Carbon Dioxide Mixing Ratio System (PGS). 2001-04-11 to 2019-07-22, Southern Great Plains (SGP) Central Facility, Lamont, OK (C1), ARM Data Center, <https://doi.org/10.5439/1025262>, 2001.
- Biraud, S., Moyes, A., and Ermold, B.: Atmospheric Radiation Measurement (ARM) user facility. Updated hourly. Flask Samplers for Carbon Cycle Gases and Isotopes (GHGFLASK). 2002-04-02 to 2019-05-23, Southern Great Plains (SGP) Central Facility, Lamont, OK (C1), ARM Data Center, <https://doi.org/10.5439/1482660>, 2002.
- Biraud, S. C., Torn, M. S., Smith, J. R., Sweeney, C., Riley, W. J., and Tans, P. P.: A multi-year record of airborne CO<sub>2</sub> observations in the US Southern Great Plains, *Atmos. Meas. Tech.*, 6, 751–763, <https://doi.org/10.5194/amt-6-751-2013>, 2013.
- Chevallier, F., Fisher, M., Peylin, P., Serrar, S., Bousquet, P., Bréon, F. M., Chédin, A., and Ciais, P.: Inferring CO<sub>2</sub> sources and sinks from satellite observations: Method and application to TOVS data, *J. Geophys. Res.-Atmos.*, 110, 1–13, <https://doi.org/10.1029/2005JD006390>, 2005.
- Chevallier, F., Bréon, F. M., and Rayner, P. J.: Contribution of the Orbiting Carbon Observatory to the estimation of CO<sub>2</sub> sources and sinks: Theoretical study in a variational data assimilation framework, *J. Geophys. Res.-Atmos.*, 112, D09307, <https://doi.org/10.1029/2006JD007375>, 2007.
- Chevallier, F., Remaud, M., O'Dell, C. W., Baker, D., Peylin, P., and Cozic, A.: Objective evaluation of surface- and satellite-driven carbon dioxide atmospheric inversions, *Atmos. Chem. Phys.*, 19, 14233–14251, <https://doi.org/10.5194/acp-19-14233-2019>, 2019.
- Ciais, P., Sabine, C., Bala, G., Bopp, L., Brovkin, V., Canadell, J., Chhabra, A., DeFries, R., Galloway, J., Heimann, M., Jones, C.,

- Quééré, C. Le, Myneni, R., Piao, S., and Thornton, P.: Carbon and Other Biogeochemical Cycles, in: *Climate Change 2013 – The Physical Science Basis*, edited by: Intergovernmental Panel on Climate Change, Cambridge University Press, Cambridge, United Kingdom and New York, NY, USA, 465–570, 2013.
- Connor, B. J., Sherlock, V., Toon, G., Wunch, D., and Wennberg, P. O.: GFIT2: an experimental algorithm for vertical profile retrieval from near-IR spectra, *Atmos. Meas. Tech.*, 9, 3513–3525, <https://doi.org/10.5194/amt-9-3513-2016>, 2016.
- Crisp, D.: NASA Orbiting Carbon Observatory: measuring the column averaged carbon dioxide mole fraction from space, *J. Appl. Remote Sens.*, 2, 023508, <https://doi.org/10.1117/1.2898457>, 2008.
- Crisp, D.: Measuring atmospheric carbon dioxide from space with the Orbiting Carbon Observatory-2 (OCO-2), in: *Earth Observing Systems XX*, edited by: Butler, J. J., Xiong, X. (Jack), and Gu, X., SPIE., vol. 9607, 960702, <https://doi.org/10.1117/12.2187291>, 2015.
- Devi, V. M., Benner, D. C., Brown, L. R., Miller, C. E., and Toth, R. A.: Line mixing and speed dependence in CO<sub>2</sub> at 6227.9 cm<sup>-1</sup>: Constrained multispectrum analysis of intensities and line shapes in the 30013 ← 00001 band, *J. Mol. Spectrosc.*, 245, 52–80, <https://doi.org/10.1016/j.jms.2007.05.015>, 2007a.
- Devi, V. M., Benner, D. C., Brown, L. R., Miller, C. E., and Toth, R. A.: Line mixing and speed dependence in CO<sub>2</sub> at 6348 cm<sup>-1</sup>: Positions, intensities, and air- and self-broadening derived with constrained multispectrum analysis, *J. Mol. Spectrosc.*, 242, 90–117, <https://doi.org/10.1016/j.jms.2007.02.018>, 2007b.
- Dlugokencky, E. J., Mund, J. W., Crotwell, A. M., Crotwell, M. J., and Thoning, K. W.: Atmospheric Carbon Dioxide Dry Air Mole Fractions from the NOAA ESRL Carbon Cycle Cooperative Global Air Sampling Network, 1968–2018, Version: 2019-07, <https://doi.org/10.15138/wkgj-f215>, 2019.
- Dohe, S.: Measurements of atmospheric CO<sub>2</sub> columns using ground-based FTIR spectra, PhD thesis, Karlsruhe Institute of Technology, Karlsruhe, Germany, 161 pp., 2013.
- Eldering, A., Taylor, T. E., O'Dell, C. W., and Pavlick, R.: The OCO-3 mission: measurement objectives and expected performance based on 1 year of simulated data, *Atmos. Meas. Tech.*, 12, 2341–2370, <https://doi.org/10.5194/amt-12-2341-2019>, 2019.
- Fletcher, R.: A modified Marquardt subroutine for non-linear least squares, Report R67, Atomic Energy Research Establishment, Harwell, Berkshire, 1971.
- Friedlingstein, P., Jones, M. W., O'Sullivan, M., Andrew, R. M., Hauck, J., Peters, G. P., Peters, W., Pongratz, J., Sitch, S., Le Quééré, C., Bakker, D. C. E., Canadell, J. G., Ciais, P., Jackson, R. B., Anthoni, P., Barbero, L., Bastos, A., Bastrikov, V., Becker, M., Bopp, L., Buitenhuis, E., Chandra, N., Chevallier, F., Chini, L. P., Currie, K. I., Feely, R. A., Gehlen, M., Gilfillan, D., Gkritzalis, T., Goll, D. S., Gruber, N., Gutekunst, S., Harris, I., Haverd, V., Houghton, R. A., Hurtt, G., Ilyina, T., Jain, A. K., Joetzer, E., Kaplan, J. O., Kato, E., Klein Goldewijk, K., Korsbakken, J. I., Landschützer, P., Lauvset, S. K., Lefèvre, N., Lenton, A., Lienert, S., Lombardozzi, D., Marland, G., McGuire, P. C., Melton, J. R., Metzl, N., Munro, D. R., Nabel, J. E. M. S., Nakaoka, S.-I., Neill, C., Omar, A. M., Ono, T., Peregon, A., Pierrot, D., Poulter, B., Rehder, G., Resplandy, L., Robertson, E., Rödenbeck, C., Séférian, R., Schwinger, J., Smith, N., Tans, P. P., Tian, H., Tilbrook, B., Tubiello, F. N., van der Werf, G. R., Wiltshire, A. J., and Zaehle, S.: Global Carbon Budget 2019, *Earth Syst. Sci. Data*, 11, 1783–1838, <https://doi.org/10.5194/essd-11-1783-2019>, 2019.
- Gordon, I. E., Rothman, L. S., Hill, C., Kochanov, R. V., Tan, Y., Bernath, P. F., Birk, M., Boudon, V., Campargue, A., Chance, K. V., Drouin, B. J., Flaud, J.-M., Gamache, R. R., Hodges, J. T., Jacquemart, D., Perevalov, V. I., Perrin, A., Shine, K. P., Smith, M.-A. H., Tennyson, J., Toon, G. C., Tran, H., Tyuterev, V. G., Barbe, A., Császár, A. G., Devi, V. M., Furtenbacher, T., Harrison, J. J., Hartmann, J.-M., Jolly, A., Johnson, T. J., Karman, T., Kleiner, I., Kyuberis, A. A., Loos, J., Lyulin, O. M., Massie, S. T., Mikhailenko, S. N., Moazzen-Ahmadi, N., Müller, H. S. P., Naumenko, O. V., Nikitin, A. V., Polyansky, O. L., Rey, M., Rotger, M., Sharpe, S. W., Sung, K., Starikova, E., Tashkun, S. A., Auwera, J. Vander, Wagner, G., Wilzewski, J., Wcisło, P., Yu, S., and Zak, E. J.: The HITRAN2016 molecular spectroscopic database, *J. Quant. Spectrosc. Radiat. Transf.*, 203, 3–69, <https://doi.org/10.1016/j.jqsrt.2017.06.038>, 2017.
- Hase, F., Hannigan, J. W., Coffey, M. T., Goldman, A., Höpfner, M., Jones, N. B., Rinsland, C. P., and Wood, S. W.: Intercomparison of retrieval codes used for the analysis of high-resolution, ground-based FTIR measurements, *J. Quant. Spectrosc. Radiat. Transf.*, 87, 25–52, <https://doi.org/10.1016/j.jqsrt.2003.12.008>, 2004.
- Karion, A., Sweeney, C., Tans, P., and Newberger, T.: AirCore: An innovative atmospheric sampling system, *J. Atmos. Ocean. Technol.*, 27, 1839–1853, <https://doi.org/10.1175/2010JTECHA1448.1>, 2010.
- Keppel-Aleks, G., Wennberg, P. O., and Schneider, T.: Sources of variations in total column carbon dioxide, *Atmos. Chem. Phys.*, 11, 3581–3593, <https://doi.org/10.5194/acp-11-3581-2011>, 2011.
- Keppel-Aleks, G., Wennberg, P. O., Washenfelder, R. A., Wunch, D., Schneider, T., Toon, G. C., Andres, R. J., Blavier, J.-F., Connor, B., Davis, K. J., Desai, A. R., Messerschmidt, J., Notholt, J., Roehl, C. M., Sherlock, V., Stephens, B. B., Vay, S. A., and Wofsy, S. C.: The imprint of surface fluxes and transport on variations in total column carbon dioxide, *Biogeosciences*, 9, 875–891, <https://doi.org/10.5194/bg-9-875-2012>, 2012.
- Keppel-Aleks, G., Wennberg, P. O., O'Dell, C. W., and Wunch, D.: Towards constraints on fossil fuel emissions from total column carbon dioxide, *Atmos. Chem. Phys.*, 13, 4349–4357, <https://doi.org/10.5194/acp-13-4349-2013>, 2013.
- Kiel, M., O'Dell, C. W., Fisher, B., Eldering, A., Nassar, R., MacDonald, C. G., and Wennberg, P. O.: How bias correction goes wrong: measurement of X<sub>CO<sub>2</sub></sub> affected by erroneous surface pressure estimates, *Atmos. Meas. Tech.*, 12, 2241–2259, <https://doi.org/10.5194/amt-12-2241-2019>, 2019.
- Kuai, L., Wunch, D., Shia, R. L., Connor, B., Miller, C., and Yung, Y.: Vertically constrained CO<sub>2</sub> retrievals from TCCON measurements, *J. Quant. Spectrosc. Radiat. Transf.*, 113, 1753–1761, <https://doi.org/10.1016/j.jqsrt.2012.04.024>, 2012.
- Kuze, A., Suto, H., Nakajima, M., and Hamazaki, T.: Thermal and near infrared sensor for carbon observation Fourier-transform spectrometer on the Greenhouse Gases Observing Satellite for greenhouse gases monitoring, *Appl. Opt.*, 48, 6716–6733, <https://doi.org/10.1364/AO.48.006716>, 2009.

- Kuze, A., Suto, H., Shiomi, K., Kawakami, S., Tanaka, M., Ueda, Y., Deguchi, A., Yoshida, J., Yamamoto, Y., Kataoka, F., Taylor, T. E., and Buijs, H. L.: Update on GOSAT TANSO-FTS performance, operations, and data products after more than 6 years in space, *Atmos. Meas. Tech.*, 9, 2445–2461, <https://doi.org/10.5194/amt-9-2445-2016>, 2016.
- Lamouroux, J., Régalia, L., Thomas, X., Vander Auwera, J., Gamache, R. R., and Hartmann, J.-M.: CO<sub>2</sub> line-mixing database and software update and its tests in the 2.1 μm and 4.3 μm regions, *J. Quant. Spectrosc. Radiat. Transf.*, 151, 88–96, <https://doi.org/10.1016/j.jqsrt.2014.09.017>, 2015.
- Laughner, J. L., Andrews, A., Roche, S., Kiel, M., Toon, G. C., Wunch, D., ACE-FTS team, ATom team, AirCore team, and Wennberg, P. O.: Revised formulation of the TCCON priors in GGG2020, in preparation, 2021a.
- Laughner, J., Andrews, A., Roche, S., Kiel, M., and Toon, G.: ginput v1.0.10: GGG2020 prior profile software (Version 1.0.10), CaltechDATA [Computer software], <https://doi.org/10.22002/D1.1944>, 2021b.
- Le Quééré, C., Andres, R. J., Boden, T., Conway, T., Houghton, R. A., House, J. I., Marland, G., Peters, G. P., van der Werf, G. R., Ahlström, A., Andrew, R. M., Bopp, L., Canadell, J. G., Ciais, P., Doney, S. C., Enright, C., Friedlingstein, P., Huntingford, C., Jain, A. K., Jourdain, C., Kato, E., Keeling, R. F., Klein Goldewijk, K., Levis, S., Levy, P., Lomas, M., Poulter, B., Raupach, M. R., Schwinger, J., Sitch, S., Stocker, B. D., Viovy, N., Zaehle, S., and Zeng, N.: The global carbon budget 1959–2011, *Earth Syst. Sci. Data*, 5, 165–185, <https://doi.org/10.5194/essd-5-165-2013>, 2013.
- Le Quééré, C., Peters, G. P., Andres, R. J., Andrew, R. M., Boden, T. A., Ciais, P., Friedlingstein, P., Houghton, R. A., Marland, G., Moriarty, R., Sitch, S., Tans, P., Arneeth, A., Arvanitis, A., Bakker, D. C. E., Bopp, L., Canadell, J. G., Chini, L. P., Doney, S. C., Harper, A., Harris, I., House, J. I., Jain, A. K., Jones, S. D., Kato, E., Keeling, R. F., Klein Goldewijk, K., Körtzinger, A., Koven, C., Lefèvre, N., Maignan, F., Omar, A., Ono, T., Park, G.-H., Pfeil, B., Poulter, B., Raupach, M. R., Regnier, P., Rödenbeck, C., Saito, S., Schwinger, J., Segschneider, J., Stocker, B. D., Takahashi, T., Tilbrook, B., van Heuven, S., Viovy, N., Wanninkhof, R., Wiltshire, A., and Zaehle, S.: Global carbon budget 2013, *Earth Syst. Sci. Data*, 6, 235–263, <https://doi.org/10.5194/essd-6-235-2014>, 2014.
- Le Quééré, C., Moriarty, R., Andrew, R. M., Peters, G. P., Ciais, P., Friedlingstein, P., Jones, S. D., Sitch, S., Tans, P., Arneeth, A., Boden, T. A., Bopp, L., Bozec, Y., Canadell, J. G., Chini, L. P., Chevallier, F., Cosca, C. E., Harris, I., Hoppema, M., Houghton, R. A., House, J. I., Jain, A. K., Johannessen, T., Kato, E., Keeling, R. F., Kitidis, V., Klein Goldewijk, K., Koven, C., Landa, C. S., Landschützer, P., Lenton, A., Lima, I. D., Marland, G., Mathis, J. T., Metzl, N., Nojiri, Y., Olsen, A., Ono, T., Peng, S., Peters, W., Pfeil, B., Poulter, B., Raupach, M. R., Regnier, P., Rödenbeck, C., Saito, S., Salisbury, J. E., Schuster, U., Schwinger, J., Séférian, R., Segschneider, J., Steinhoff, T., Stocker, B. D., Sutton, A. J., Takahashi, T., Tilbrook, B., van der Werf, G. R., Viovy, N., Wang, Y.-P., Wanninkhof, R., Wiltshire, A., and Zeng, N.: Global carbon budget 2014, *Earth Syst. Sci. Data*, 7, 47–85, <https://doi.org/10.5194/essd-7-47-2015>, 2015a.
- Le Quééré, C., Moriarty, R., Andrew, R. M., Canadell, J. G., Sitch, S., Korsbakken, J. I., Friedlingstein, P., Peters, G. P., Andres, R. J., Boden, T. A., Houghton, R. A., House, J. I., Keeling, R. F., Tans, P., Arneeth, A., Bakker, D. C. E., Barbero, L., Bopp, L., Chang, J., Chevallier, F., Chini, L. P., Ciais, P., Fader, M., Feely, R. A., Gkritzalis, T., Harris, I., Hauck, J., Ilyina, T., Jain, A. K., Kato, E., Kitidis, V., Klein Goldewijk, K., Koven, C., Landschützer, P., Lauvset, S. K., Lefèvre, N., Lenton, A., Lima, I. D., Metzl, N., Millero, F., Munro, D. R., Murata, A., Nabel, J. E. M. S., Nakaoka, S., Nojiri, Y., O'Brien, K., Olsen, A., Ono, T., Pérez, F. F., Pfeil, B., Pierrot, D., Poulter, B., Rehder, G., Rödenbeck, C., Saito, S., Schuster, U., Schwinger, J., Séférian, R., Steinhoff, T., Stocker, B. D., Sutton, A. J., Takahashi, T., Tilbrook, B., van der Laan-Luijkx, I. T., van der Werf, G. R., van Heuven, S., Vandemark, D., Viovy, N., Wiltshire, A., Zaehle, S., and Zeng, N.: Global Carbon Budget 2015, *Earth Syst. Sci. Data*, 7, 349–396, <https://doi.org/10.5194/essd-7-349-2015>, 2015b.
- Le Quééré, C., Andrew, R. M., Canadell, J. G., Sitch, S., Korsbakken, J. I., Peters, G. P., Manning, A. C., Boden, T. A., Tans, P. P., Houghton, R. A., Keeling, R. F., Alin, S., Andrews, O. D., Anthoni, P., Barbero, L., Bopp, L., Chevallier, F., Chini, L. P., Ciais, P., Currie, K., Delire, C., Doney, S. C., Friedlingstein, P., Gkritzalis, T., Harris, I., Hauck, J., Haverd, V., Hoppema, M., Klein Goldewijk, K., Jain, A. K., Kato, E., Körtzinger, A., Landschützer, P., Lefèvre, N., Lenton, A., Lienert, S., Lombardozi, D., Melton, J. R., Metzl, N., Millero, F., Monteiro, P. M. S., Munro, D. R., Nabel, J. E. M. S., Nakaoka, S., O'Brien, K., Olsen, A., Omar, A. M., Ono, T., Pierrot, D., Poulter, B., Rödenbeck, C., Salisbury, J., Schuster, U., Schwinger, J., Séférian, R., Skjelvan, I., Stocker, B. D., Sutton, A. J., Takahashi, T., Tian, H., Tilbrook, B., van der Laan-Luijkx, I. T., van der Werf, G. R., Viovy, N., Walker, A. P., Wiltshire, A. J., and Zaehle, S.: Global Carbon Budget 2016, *Earth Syst. Sci. Data*, 8, 605–649, <https://doi.org/10.5194/essd-8-605-2016>, 2016.
- Le Quééré, C., Andrew, R. M., Friedlingstein, P., Sitch, S., Pongratz, J., Manning, A. C., Korsbakken, J. I., Peters, G. P., Canadell, J. G., Jackson, R. B., Boden, T. A., Tans, P. P., Andrews, O. D., Arora, V. K., Bakker, D. C. E., Barbero, L., Becker, M., Betts, R. A., Bopp, L., Chevallier, F., Chini, L. P., Ciais, P., Cosca, C. E., Cross, J., Currie, K., Gasser, T., Harris, I., Hauck, J., Haverd, V., Houghton, R. A., Hunt, C. W., Hurtt, G., Ilyina, T., Jain, A. K., Kato, E., Kautz, M., Keeling, R. F., Klein Goldewijk, K., Körtzinger, A., Landschützer, P., Lefèvre, N., Lenton, A., Lienert, S., Lima, I., Lombardozi, D., Metzl, N., Millero, F., Monteiro, P. M. S., Munro, D. R., Nabel, J. E. M. S., Nakaoka, S., Nojiri, Y., Padin, X. A., Peregón, A., Pfeil, B., Pierrot, D., Poulter, B., Rehder, G., Reimer, J., Rödenbeck, C., Schwinger, J., Séférian, R., Skjelvan, I., Stocker, B. D., Tian, H., Tilbrook, B., Tubiello, F. N., van der Laan-Luijkx, I. T., van der Werf, G. R., van Heuven, S., Viovy, N., Vuichard, N., Walker, A. P., Watson, A. J., Wiltshire, A. J., Zaehle, S., and Zhu, D.: Global Carbon Budget 2017, *Earth Syst. Sci. Data*, 10, 405–448, <https://doi.org/10.5194/essd-10-405-2018>, 2018a.
- Le Quééré, C., Andrew, R. M., Friedlingstein, P., Sitch, S., Hauck, J., Pongratz, J., Pickers, P. A., Korsbakken, J. I., Peters, G. P., Canadell, J. G., Arneeth, A., Arora, V. K., Barbero, L., Bastos, A., Bopp, L., Chevallier, F., Chini, L. P., Ciais, P., Doney, S. C., Gkritzalis, T., Goll, D. S., Harris, I., Haverd, V., Hoffman, F. M., Hoppema, M., Houghton, R. A., Hurtt, G., Ilyina, T., Jain, A. K., Johannessen, T., Jones, C. D., Kato, E., Keeling, R. F., Goldewijk, K. K., Landschützer, P., Lefèvre, N., Lienert, S., Liu, Z.,

- Lombardozi, D., Metzl, N., Munro, D. R., Nabel, J. E. M. S., Nakaoka, S., Neill, C., Olsen, A., Ono, T., Patra, P., Peregon, A., Peters, W., Peylin, P., Pfeil, B., Pierrot, D., Poulter, B., Rehder, G., Resplandy, L., Robertson, E., Rocher, M., Rödenbeck, C., Schuster, U., Schwinger, J., Séférian, R., Skjelvan, I., Steinhoff, T., Sutton, A., Tans, P. P., Tian, H., Tilbrook, B., Tubiello, F. N., van der Laan-Luijkx, I. T., van der Werf, G. R., Viovy, N., Walker, A. P., Wiltshire, A. J., Wright, R., Zaehle, S., and Zheng, B.: Global Carbon Budget 2018, *Earth Syst. Sci. Data*, 10, 2141–2194, <https://doi.org/10.5194/essd-10-2141-2018>, 2018b.
- Liu, Y., Wang, J., Yao, L., Chen, X., Cai, Z., Yang, D., Yin, Z., Gu, S., Tian, L., Lu, N., and Lyu, D.: The TanSat mission: preliminary global observations, *Sci. Bull.*, 63, 1200–1207, <https://doi.org/10.1016/j.scib.2018.08.004>, 2018.
- Lucchesi, R.: File Specification for GEOS-5 FP-IT (forward processing for instrument teams), Tech. rep., NASA Goddard Space Flight Center, Greenbelt, MD, USA, available at: <https://gmao.gsfc.nasa.gov/pubs/docs/Lucchesi865.pdf> (last access: 13 October 2020), 2015.
- McKenna, D. S., Konopka, P., Groöß, J.-U., Günther, G., Müller, R., Spang, R., Offermann, D., and Orsolini, Y.: A new Chemical Lagrangian Model of the Stratosphere (CLaMS) 1. Formulation of advection and mixing, *J. Geophys. Res.*, 107, 4309, <https://doi.org/10.1029/2000jd000114>, 2002.
- Mendonca, J., Strong, K., Toon, G. C., Wunch, D., Sung, K., Deutscher, N. M., Griffith, D. W. T., and Franklin, J. E.: Improving atmospheric CO<sub>2</sub> retrievals using line mixing and speed-dependence when fitting high-resolution ground-based solar spectra, *J. Mol. Spectrosc.*, 323, 15–27, <https://doi.org/10.1016/j.jms.2016.01.007>, 2016.
- Mendonca, J., Strong, K., Sung, K., Devi, V. M., Toon, G. C., Wunch, D., and Franklin, J. E.: Using high-resolution laboratory and ground-based solar spectra to assess CH<sub>4</sub> absorption coefficient calculations, *J. Quant. Spectrosc. Radiat. Transf.*, 190, 48–59, <https://doi.org/10.1016/j.jqsrt.2016.12.013>, 2017.
- Mendonca, J., Strong, K., Wunch, D., Toon, G. C., Long, D. A., Hodges, J. T., Sironneau, V. T., and Franklin, J. E.: Using a speed-dependent Voigt line shape to retrieve O<sub>2</sub> from Total Carbon Column Observing Network solar spectra to improve measurements of XCO<sub>2</sub>, *Atmos. Meas. Tech.*, 12, 35–50, <https://doi.org/10.5194/amt-12-35-2019>, 2019.
- Myhre, G., Shindell, D., Bréon, F., Collins, W., Fuglestedt, J., Huang, J., Koch, D., Lamarque, J., Lee, D., Mendoza, B., Nakajima, T., Robock, A., Stephens, G., Takemura, T., and Zhan, H.: Anthropogenic and Natural Radiative Forcing, in: *Climate Change 2013 – The Physical Science Basis*, edited by: Intergovernmental Panel on Climate Change, Cambridge University Press, Cambridge, United Kingdom and New York, NY, USA, 659–740, 2013.
- Nakajima, M., Kuze, A., and Suto, H.: The current status of GOSAT and the concept of GOSAT-2, in: *Sensors, Systems, and Next-Generation Satellites XVI*, edited by: Meynart, R., Neeck, S. P., and Shimoda, H., SPIE., 8533, 21–30, <https://doi.org/10.1117/12.974954>, 2012.
- O'Dell, C. W., Eldering, A., Wennberg, P. O., Crisp, D., Gunson, M. R., Fisher, B., Frankenberg, C., Kiel, M., Lindqvist, H., Mandrake, L., Merrelli, A., Natraj, V., Nelson, R. R., Osterman, G. B., Payne, V. H., Taylor, T. E., Wunch, D., Drouin, B. J., Oyafuso, F., Chang, A., McDuffie, J., Smyth, M., Baker, D. F., Basu, S., Chevallier, F., Crowell, S. M. R., Feng, L., Palmer, P. I., Dubey, M., García, O. E., Griffith, D. W. T., Hase, F., Iraci, L. T., Kivi, R., Morino, I., Notholt, J., Ohyama, H., Petri, C., Roehl, C. M., Sha, M. K., Strong, K., Sussmann, R., Te, Y., Uchino, O., and Velasco, V. A.: Improved retrievals of carbon dioxide from Orbiting Carbon Observatory-2 with the version 8 ACOS algorithm, *Atmos. Meas. Tech.*, 11, 6539–6576, <https://doi.org/10.5194/amt-11-6539-2018>, 2018.
- Parazoo, N. C., Denning, A. S., Kawa, S. R., Pawson, S., and Lokupitiya, R.: CO<sub>2</sub> flux estimation errors associated with moist atmospheric processes, *Atmos. Chem. Phys.*, 12, 6405–6416, <https://doi.org/10.5194/acp-12-6405-2012>, 2012.
- Peters, W., Jacobson, A. R., Sweeney, C., Andrews, A. E., Conway, T. J., Masarie, K., Miller, J. B., Bruhwiler, L. M. P., Petron, G., Hirsch, A. L., Worthy, D. E. J., van der Werf, G. R., Randerson, J. T., Wennberg, P. O., Krol, M. C., and Tans, P. P.: An atmospheric perspective on North American carbon dioxide exchange: CarbonTracker, *Proc. Natl. Acad. Sci.*, 104, 18925–18930, <https://doi.org/10.1073/pnas.0708986104>, 2007.
- Pickett-Heaps, C. A., Rayner, P. J., Law, R. M., Ciais, P., Patra, P. K., Bousquet, P., Peylin, P., Maksyutov, S., Marshall, J., Rödenbeck, C., Langenfelds, R. L., Steele, L. P., Francey, R. J., Tans, P., and Sweeney, C.: Atmospheric CO<sub>2</sub> inversion validation using vertical profile measurements: Analysis of four independent inversion models, *J. Geophys. Res.*, 116, D12305, <https://doi.org/10.1029/2010JD014887>, 2011.
- Rayner, P. J., and O'Brien, D. M.: The utility of remotely sensed CO<sub>2</sub> concentration data in surface source inversions, *Geophys. Res. Lett.*, 28, 175–178, <https://doi.org/10.1029/2000GL011912>, 2001.
- Rödenbeck, C., Houweling, S., Gloor, M., and Heimann, M.: CO<sub>2</sub> flux history 1982–2001 inferred from atmospheric data using a global inversion of atmospheric transport, *Atmos. Chem. Phys.*, 3, 1919–1964, <https://doi.org/10.5194/acp-3-1919-2003>, 2003.
- Rodgers, C. D.: Characterization and error analysis of profiles retrieved from remote sounding measurements, *J. Geophys. Res.*, 95, 5587–5595, <https://doi.org/10.1029/JD095iD05p05587>, 1990.
- Rodgers, C. D.: *Inverse Methods for Atmospheric Sounding: Theory and Practice*, World Scientific, Singapore, 2000.
- Rodgers, C. D. and Connor, B. J.: Intercomparison of remote sounding instruments, *J. Geophys. Res.-Atmos.*, 108, 4116, <https://doi.org/10.1029/2002JD002299>, 2003.
- Rosenkranz, P.: Shape of the 5 mm oxygen band in the atmosphere, *IEEE Trans. Antennas Propag.*, 23, 498–506, <https://doi.org/10.1109/TAP.1975.1141119>, 1975.
- Rothman, L. S., Jacquemart, D., Barbe, A., Benner, D. C., Birk, M., Brown, L. R., Carleer, M. R., Chackerian, C., Chance, K., Coudert, L. H., Dana, V., Devi, V. M., Flaud, J. M., Gamache, R. R., Goldman, A., Hartmann, J. M., Jucks, K. W., Maki, A. G., Mandin, J. Y., Massie, S. T., Orphal, J., Perrin, A., Rinsland, C. P., Smith, M. A. H., Tennyson, J., Tolchenov, R. N., Toth, R. A., Vander Auwera, J., Varanasi, P., and Wagner, G.: The HITRAN 2004 molecular spectroscopic database, *J. Quant. Spectrosc. Radiat. Transf.*, 96, 139–204, <https://doi.org/10.1016/j.jqsrt.2004.10.008>, 2005.
- Rothman, L. S., Gordon, I. E., Barbe, A., Benner, D. C., Bernath, P. F., Birk, M., Boudon, V., Brown, L. R., Campargue, A., Champion, J. P., Chance, K., Coudert, L. H., Dana, V., Devi,

- V. M., Fally, S., Flaud, J. M., Gamache, R. R., Goldman, A., Jacquemart, D., Kleiner, I., Lacombe, N., Lafferty, W. J., Mandin, J. Y., Massie, S. T., Mikhailenko, S. N., Miller, C. E., Moazzen-Ahmadi, N., Naumenko, O. V., Nikitin, A. V., Orphal, J., Perevalov, V. I., Perrin, A., Predoi-Cross, A., Rinsland, C. P., Rotger, M., Šimečková, M., Smith, M. A. H., Sung, K., Tashkun, S. A., Tennyson, J., Toth, R. A., Vandaele, A. C., and Vander Auwera, J.: The HITRAN 2008 molecular spectroscopic database, *J. Quant. Spectrosc. Radiat. Transf.*, 110, 533–572, <https://doi.org/10.1016/j.jqsrt.2009.02.013>, 2009.
- Rothman, L. S., Gordon, I. E., Babikov, Y., Barbe, A., Chris Benner, D., Bernath, P. F., Birk, M., Bizzocchi, L., Boudon, V., Brown, L. R., Campargue, A., Chance, K., Cohen, E. A., Coudert, L. H., Devi, V. M., Drouin, B. J., Fayt, A., Flaud, J. M., Gamache, R. R., Harrison, J. J., Hartmann, J. M., Hill, C., Hodges, J. T., Jacquemart, D., Jolly, A., Lamouroux, J., Le Roy, R. J., Li, G., Long, D. A., Lyulin, O. M., Mackie, C. J., Massie, S. T., Mikhailenko, S., Müller, H. S. P., Naumenko, O. V., Nikitin, A. V., Orphal, J., Perevalov, V., Perrin, A., Polovtseva, E. R., Richard, C., Smith, M. A. H., Starikova, E., Sung, K., Tashkun, S., Tennyson, J., Toon, G. C., Tyuterev, V. G., and Wagner, G.: The HITRAN2012 molecular spectroscopic database, *J. Quant. Spectrosc. Radiat. Transf.*, 130, 4–50, <https://doi.org/10.1016/j.jqsrt.2013.07.002>, 2013.
- Saeki, T. and Patra, P. K.: Implications of overestimated anthropogenic CO<sub>2</sub> emissions on East Asian and global land CO<sub>2</sub> flux inversion, *Geosci. Lett.*, 4, 9, <https://doi.org/10.1186/s40562-017-0074-7>, 2017.
- Stephens, B. B., Gurney, K. R., Tans, P. P., Sweeney, C., Peters, W., Bruhwiler, L., Ciais, P., Ramonet, M., Bousquet, P., Nakazawa, T., Aoki, S., Machida, T., Inoue, G., Vinnichenko, N., Lloyd, J., Jordan, A., Heimann, M., Shibistova, O., Langenfelds, R. L., Steele, L. P., Francey, R. J., and Denning, A. S.: Weak Northern and Strong Tropical Land Carbon Uptake from Vertical Profiles of Atmospheric CO<sub>2</sub>, *Science*, 316, 1732–1735, <https://doi.org/10.1126/science.1137004>, 2007.
- Sweeney, C., Higgs, J., Wolter, S., Crotwell, A., Neff, D., Dlugokencky, E., Lang, P., Novelli, P., Mund, J., Moglia, E., and Crotwell, M.: Earth System Research Laboratory Carbon Cycle and Greenhouse Gases Group Flask-Air Sample Measurements of CO<sub>2</sub>, CH<sub>4</sub>, CO, N<sub>2</sub>O, H<sub>2</sub>, and SF<sub>6</sub> from the Aircraft Program, 1992–Present, Version 1, NOAA National Centers for Environmental Information, <https://doi.org/10.7289/V5N58JMF>, 2017.
- Tange, O.: GNU Parallel – The Command-Line Power Tool, *USENIX Mag.*, 36, 42–47, Zenodo, <https://doi.org/10.5281/zenodo.16303>, 2011.
- Toon, G. C.: Atmospheric Line List for the 2014 TCCON Data Release (Version GGG2014.R0) [Data set], CaltechDATA, <https://doi.org/10.14291/tcon.ggg2014.atm.r0/1221656>, 2015.
- Toon, G. C., Blavier, J.-F., Sung, K., Rothman, L. S., and E. Gordon, I.: HITRAN spectroscopy evaluation using solar occultation FTIR spectra, *J. Quant. Spectrosc. Radiat. Transf.*, 182, 324–336, <https://doi.org/10.1016/j.jqsrt.2016.05.021>, 2016.
- Toth, R. A., Brown, L. R., Miller, C. E., Malathy Devi, V., and Benner, D. C.: Spectroscopic database of CO<sub>2</sub> line parameters: 4300–7000 cm<sup>-1</sup>, *J. Quant. Spectrosc. Radiat. Transf.*, 109, 906–921, <https://doi.org/10.1016/j.jqsrt.2007.12.004>, 2008.
- van der Laan-Luijkx, I. T., van der Velde, I. R., van der Veen, E., Tsuruta, A., Stanislawski, K., Babenhauserheide, A., Zhang, H. F., Liu, Y., He, W., Chen, H., Masarie, K. A., Krol, M. C., and Peters, W.: The CarbonTracker Data Assimilation Shell (CTDAS) v1.0: implementation and global carbon balance 2001–2015, *Geosci. Model Dev.*, 10, 2785–2800, <https://doi.org/10.5194/gmd-10-2785-2017>, 2017.
- Wennberg, P. O., Wunch, D., Roehl, C. M., Blavier, J.-F., Toon, G. C., and Allen, N. T.: TCCON data from Lamont (US), Release GGG2014.R1 [Data set], CaltechDATA, <https://doi.org/10.14291/tcon.ggg2014.lamont01.r1/1255070>, 2016.
- Wofsy, S. C.: HIAPER Pole-to-Pole Observations (HIPPO): fine-grained, global-scale measurements of climatically important atmospheric gases and aerosols, *Philos. Trans. R. Soc. A Math. Phys. Eng. Sci.*, 369, 2073–2086, <https://doi.org/10.1098/rsta.2010.0313>, 2011.
- Wofsy, S. C., Afshar, S., Allen, H. M., Apel, E., Asher, E. C., Barletta, B., Bent, J., Bian, H., Biggs, B. C., Blake, D. R., Blake, N., Bourgeois, I., Brock, C. A., Brune, W. H., Budney, J. W., Bui, T. P., Butler, A., Campuzano-Jost, P., Chang, C. S., Chin, M., Commane, R., Correa, G., Crounse, J. D., Cullis, P. D., Daube, B. C., Day, D. A., Dean-Day, J. M., Dibb, J. E., Disingangi, J. P., Diskin, G. S., Dollner, M., Elkins, J. W., Erdesz, F., Fiore, A. M., Flynn, C. M., Froyd, K., Gesler, D. W., Hall, S. R., Hanisco, T. F., Hannun, R. A., Hills, A. J., Hints, E. J., Hoffman, A., Hornbrook, R. S., Huey, L. G., Hughes, S., Jimenez, J. L., Johnson, B. J., Katich, J. M., Keeling, R., Kim, M. J., Kupc, A., Lait, L. R., Lamarque, J.-F., Liu, J., McKain, K., McLaughlin, R. J., Meinardi, S., Miller, D. O., Montzka, S. A., Moore, F. L., Morgan, E. J., Murphy, D. M., Murray, L. T., Nault, B. A., Neuman, J. A., Newman, P. A., Nicely, J. M., Pan, X., Paplawsky, W., Peischl, J., Prather, M. J., Price, D. J., Ray, E., Reeves, J. M., Richardson, M., Rollins, A. W., Rosenlof, K. H., Ryerson, T. B., Scheuer, E., Schill, G. P., Schroder, J. C., Schwarz, J. P., St.Clair, J. M., Steenrod, S. D., Stephens, B. B., Strode, S. A., Sweeney, C., Tanner, D., Teng, A. P., Thames, A. B., Thompson, C. R., Ullmann, K., Veres, P. R., Vizenor, N., Wagner, N. L., Watt, A., Weber, R., Weinzierl, B., Wennberg, P. O., Williamson, C. J., Wilson, J. C., Wolfe, G. M., Woods, C. T., and Zeng, L. H.: ATom: Merged Atmospheric Chemistry, Trace Gases, and Aerosols, ORNL DAAC, Oak Ridge, Tennessee, USA, <https://doi.org/10.3334/ORNLDAAC/1581>, 2018.
- Wunch, D., Toon, G. C., Wennberg, P. O., Wofsy, S. C., Stephens, B. B., Fischer, M. L., Uchino, O., Abshire, J. B., Bernath, P., Biraud, S. C., Blavier, J.-F. L., Boone, C., Bowman, K. P., Browell, E. V., Campos, T., Connor, B. J., Daube, B. C., Deutscher, N. M., Diao, M., Elkins, J. W., Gerbig, C., Gottlieb, E., Griffith, D. W. T., Hurst, D. F., Jiménez, R., Keppel-Aleks, G., Kort, E. A., Macatangay, R., Machida, T., Matsueda, H., Moore, F., Morino, I., Park, S., Robinson, J., Roehl, C. M., Sawa, Y., Sherlock, V., Sweeney, C., Tanaka, T., and Zondlo, M. A.: Calibration of the Total Carbon Column Observing Network using aircraft profile data, *Atmos. Meas. Tech.*, 3, 1351–1362, <https://doi.org/10.5194/amt-3-1351-2010>, 2010.
- Wunch, D., Wennberg, P. O., Toon, G. C., Connor, B. J., Fisher, B., Osterman, G. B., Frankenberg, C., Mandrake, L., O'Dell, C., Ahonen, P., Biraud, S. C., Castano, R., Cressie, N., Crisp, D., Deutscher, N. M., Eldering, A., Fisher, M. L., Griffith, D. W. T., Gunson, M., Heikkinen, P., Keppel-Aleks, G., Kyrö, E., Lindenmaier, R., Macatangay, R., Mendonca, J., Messer-

- schmidt, J., Miller, C. E., Morino, I., Notholt, J., Oyafuso, F. A., Rettinger, M., Robinson, J., Roehl, C. M., Salawitch, R. J., Sherlock, V., Strong, K., Sussmann, R., Tanaka, T., Thompson, D. R., Uchino, O., Warneke, T., and Wofsy, S. C.: A method for evaluating bias in global measurements of CO<sub>2</sub> total columns from space, *Atmos. Chem. Phys.*, 11, 12317–12337, <https://doi.org/10.5194/acp-11-12317-2011>, 2011a.
- Wunch, D., Toon, G. C., Blavier, J.-F. L., Washenfelder, R. A., Notholt, J., Connor, B. J., Griffith, D. W. T., Sherlock, V., and Wennberg, P. O.: The Total Carbon Column Observing Network, *Philos. Trans. R. Soc. A Math. Phys. Eng. Sci.*, 369, 2087–2112, <https://doi.org/10.1098/rsta.2010.0240>, 2011b.
- Wunch, D., Toon, G. C., Sherlock, V., Deutscher, N. M., Liu, C., Feist, D. G., and Wennberg, P. O.: Documentation for the 2014 TCCON Data Release (Version GGG2014.R0), CaltechDATA, <https://doi.org/10.14291/tccon.ggg2014.documentation.r0/1221662>, 2015.
- Wunch, D., Wennberg, P. O., Osterman, G., Fisher, B., Naylor, B., Roehl, C. M., O'Dell, C., Mandrake, L., Viatte, C., Kiel, M., Griffith, D. W. T., Deutscher, N. M., Velasco, V. A., Notholt, J., Warneke, T., Petri, C., De Maziere, M., Sha, M. K., Sussmann, R., Rettinger, M., Pollard, D., Robinson, J., Morino, I., Uchino, O., Hase, F., Blumenstock, T., Feist, D. G., Arnold, S. G., Strong, K., Mendonca, J., Kivi, R., Heikkinen, P., Iraci, L., Podolske, J., Hillyard, P. W., Kawakami, S., Dubey, M. K., Parker, H. A., Sepulveda, E., García, O. E., Te, Y., Jeseck, P., Gunson, M. R., Crisp, D., and Eldering, A.: Comparisons of the Orbiting Carbon Observatory-2 (OCO-2) X<sub>CO<sub>2</sub></sub> measurements with TCCON, *Atmos. Meas. Tech.*, 10, 2209–2238, <https://doi.org/10.5194/amt-10-2209-2017>, 2017.
- Wunch, D., Mendonca, J., Colebatch, O., Allen, N. T., Blavier, J.-F., Roche, S., Hedelius, J., Neufeld, G., Springett, S., Worthy, D., Kessler, R., and Strong, K.: TCCON data from East Trout Lake, SK (CA), Release GGG2014.R1 [Data set], CaltechDATA, <https://doi.org/10.14291/tccon.ggg2014.eastroutlake01.r1>, 2018.